



PhD Title

PhD Thesis

D. Maciver

Chemical and Process Engineering Department

University of Strathclyde, Glasgow

July 11, 2024

This thesis is the result of the author's original research. It has been composed by the author and has not been previously submitted for examination which has led to the award of a degree.

The copyright of this thesis belongs to the author under the terms of the United Kingdom Copyright Acts as qualified by University of Strathclyde Regulation 3.50. Due acknowledgement must always be made of the use of any material contained in, or derived from, this thesis.

# **Abstract**

# Contents

<b>Abstract</b>	<b>ii</b>
<b>List of Figures</b>	<b>vi</b>
<b>List of Tables</b>	<b>xiii</b>
<b>Preface/Acknowledgements</b>	<b>xv</b>
<b>1 Introduction</b>	<b>2</b>
1.1 Nucleation . . . . .	3
1.1.1 Primary vs Secondary nucleation . . . . .	4
1.2 Nucleation Theories . . . . .	5
1.2.1 Classical Nucleation Theory (CNT) . . . . .	5
1.2.2 Two Step Nucleation . . . . .	9
1.3 Crystallisation methods . . . . .	10
1.3.1 Cooling Crystallisation . . . . .	10
1.4 Optical Tweezers . . . . .	12
1.4.1 Background . . . . .	12

## Contents

1.4.2	Literature related to laser induced nucleation . . . . .	12
1.4.3	Optical Rotation . . . . .	14
1.4.4	Shear induced Nucleation . . . . .	17
1.5	Aims and Objectives . . . . .	18
<b>2</b>	<b>Theory and methods</b>	<b>20</b>
2.1	Working Principle . . . . .	20
2.2	Electromagnetism and optical tweezing . . . . .	22
2.2.1	Ray-Optics Regime . . . . .	24
2.2.2	Lornez-Mie Theory . . . . .	25
2.2.3	Rayleigh Regime . . . . .	27
2.3	Scattering methods . . . . .	28
2.3.1	T-matrix Method . . . . .	29
2.3.2	Discrete Dipole Approximation . . . . .	30
2.4	Langevin Equation . . . . .	31
2.4.1	Finite Difference . . . . .	33
2.5	Calibration Techniques . . . . .	35
2.5.1	Potential Well Analysis . . . . .	36
2.5.2	Equipartition method . . . . .	38
2.5.3	Mean Square Displacement . . . . .	38
2.5.4	Power Spectrum Density (PSD) . . . . .	42
2.6	Simulation of spherical aggregates . . . . .	45
2.6.1	Simulated Quadrant Photodiode . . . . .	48

## Contents

<b>3 Effects of localised shearing on crystal growth and nucleation</b>	<b>52</b>
3.1 Optical Tweezer Equipment . . . . .	53
3.1.1 Position detection methods . . . . .	54
3.1.2 Fourier Optics and 4f correlators . . . . .	57
3.2 Calibration of Tweezer Setup . . . . .	58
3.3 Synthesis of Birefringent Micro spheres . . . . .	58
3.3.1 Rotation of birefringent micro spheres . . . . .	61
3.4 Rotation of micro-rotors in supersaturated solutions . . . . .	64
3.5 Shearing via a Galvano-mirror . . . . .	66
3.6 Nucleation using a moving beam . . . . .	67
<b>4 Complex Langevin dynamics of spherical dimers</b>	<b>69</b>
4.1 Positional and Orientational dependence of Trapping forces . . . . .	70
4.1.1 Non-trivial harmonic traps . . . . .	73
4.2 Continuous rotational motion due to second-order scattering . . . . .	75
4.2.1 Gyroscopic Precession using asymmetric dimers . . . . .	81
4.3 Characterisation of asymmetric dimers via PSD analysis . . . . .	83
4.4 Conclusions . . . . .	85
<b>5 Detection and Characterisation of rotational spherical aggregate rotational dynamics</b>	<b>87</b>
5.1 Simulative QPD . . . . .	87
5.1.1 Incident beam . . . . .	87
5.1.2 Scattered and Total Fields . . . . .	90

## Contents

5.2	Rotations and Asymmetric particles . . . . .	94
5.3	Power Spectra of single sphere vs spherical aggregates . . . . .	95
5.4	Monitoring Stochastic rotational motion using static light scattering . .	97
5.4.1	Coordinate System . . . . .	97
5.4.2	Dimer . . . . .	97
5.4.3	Beam . . . . .	98
5.4.4	Detectors and Pixels . . . . .	98
5.5	Interpretation of scattering data into orientation estimates . . . . .	99
<b>6</b>	<b>Closing Remarks</b>	<b>100</b>
<b>A</b>	<b>Stuff That Didn't Fit Anywhere Else</b>	<b>101</b>
	<b>Bibliography</b>	<b>101</b>

# List of Figures

1.1	Secondary Nucleation mechanisms, classified by Agrawal and Paterson [1]	5
1.2	Free energy diagram of a newly formed nucleus according to the Classical Nucleation Theory. The total free energy (blue) is due to the competition between the volume free energy gain (green) and the interfacial free energy cost (orange). Dotted lines are for a higher supersaturation than the solid lines, the interfacial energy cost is independent of supersaturation.	7
1.3	Typical Concentration vs Temperature plot with the solubility curve (black) and metastable zone (red). 3 different cooling curves are shown as well: a high rate of cooling (orange) shows the mixture quickly dropping below the solubility curve resulting in no new nuclei forming; a low rate of cooling (green) shows the mixture exceeding the metastable zone, where now nucleation occurs freely; and a typical cooling rate (blue) shows how a typical cooling crystalliser will operate, sitting in the middle of the other two curves.	11

## List of Figures

2.1 Working principle for an optical trap, upper image shows a sphere at the centre of a trap experiences equal forces directed towards inwards. Lower image shows that when displaced 'ray a' is refracted far more than 'ray b' resulting in a net force back towards the centre. . . . .	21
2.2 Example trajectory created using Finite Differences method for a $2\mu m$ diameter sphere. Trap stiffness's were estimated using <i>ott</i> at $\kappa_x = \kappa_y = -100 \text{ pN}/\mu m$ and $\kappa_z = -25 \text{ pN}/\mu m$ . The particle's motion can be localised around the shaded ellipsoid. . . . .	36
2.3 Example mean squared displacement using eq. 2.40, for a $1\mu m$ sphere trapped by an optical potential well. The dotted line represents the upper limit of the sphere's displacement due to the optical trap. . . . .	40
2.4 Example PSD fitted using Eq. 2.44, power spectra is collected from an optically trapped silica sphere suspended in water. The difference in magnitude is due to the asymmetry of the quadrant photo diode having a stronger signal response in the direction of the polarisation vector. Using a correction factor (see Eq. 2.46) will adjust the power spectra to better describe the trap shape. . . . .	43

## List of Figures

2.5 Total Field incident on the quadrant photo diode for a several different displacements. Top Left: $2\mu m$ diameter silica sphere placed at the focus of a beam. Top Right: silica sphere is now displaced by $1\mu m$ along the x-axis. Bottom Right: silica sphere is now displaced by $1\mu m$ along the y-axis. Bottom Left: silica sphere is now displaced by $0.707\mu m$ along the x and y axis. The trapping beam is a $TEM_{00}$ Gaussian, polarised along the along the x-axis. $S_x$ , $S_y$ , and $S_z$ are shown to the right of each graph, $Q_1$ , $Q_2$ , $Q_3$ , and $Q_4$ are shown above each graph. . . . .	50
2.6 Comparison between QPD response signal versus work conducted by Rohrbach, single sphere ( $r = 150 nm$ , $n = 1.57$ ) is scanned by a $1064 nm$ laser and the QPD signal recorded. Solid lines represent the signal produced by QPD using <i>ott</i> and points represent the signal response collected from [2]. . . . .	51
3.1 Optical tweezer set up used for the majority of the PhD. The focal lengths of $f_1$ , $f_2$ , $f_3$ , & $f_4$ are $-20 mm$ , $60 mm$ , $150 mm$ , & $200 mm$ respectively. Diagram not drawn to scale. . . . .	55
3.2 Comparison between QPD and Lateral effect photodiodes. The four quadrants of a QPD (left) experience different photocurrents based on the total intensity of light incident on each section (labelled A, B, C, D). Whereas a Lateral effect sensor (right) uses the resistive properties of the photodiode surface to vary the create different photocurrents passing through the anodes A, B, C, and D. . . . .	57

## List of Figures

3.3 (a) Sample vaterite sphere suspended in water and trapped by circular polarised trap. (b) Collected power spectrum from rotating vaterite, peaks in the power spectrum appear at integer multiples of the rotational frequency ( $f_{rot} \approx 49.8$ Hz) . . . . .	60
3.4 Liquid crystal undergoing rotation due to the circularly polarised trap. .	61
3.5 (a) Fluid flow radiating out from the surface of a rotating vaterite sphere.	
(b) Shear rates computed using Eq.3.4, optimal shear rate is of $3000s^{-1}$ is indicated by the dotted line. Vaterite radii and rotation frequencies are shown, the laser power was kept constant at 450 mW. Reported rotation rates, and their corresponding fluid flow and shear rates, for vaterite are also plotted alongside lab results. . . . .	63
3.6 Diagram of optical trapping set up for rotating birefringent particles in a supersaturated solution. Left: side view of the trapping set up showing the location of the trap focus at the edge of the droplet of a supersaturated solution. Right: top down view of the glycine droplet with a trapped birefringent particle shown close to edge of the trap. As the particle rotates the drag force from the surrounding fluid generates a flow field around itself (see Eq. 3.3). . . . .	65

## List of Figures

4.1 Plots of force vs displacement of the point of the contact of the spheres ( $\mu\text{m}$ ) for the case of a dimer of size ratio 2. (a) is the case where the smaller sphere is orientated with the beam propagation direction. (b) is the inverted case, smaller sphere oriented against the propagation direction. Renders to visualise the dimer orientation are shown below each plot. The black lines on each force-curve is a linear fit with the slope being reported as the trap stiffness in the legend. . . . .	71
4.2 Plots of force vs displacement of the point of the contact of the spheres ( $\mu\text{m}$ ) for the case of a dimer of size ratio 2 while being displaced in the transverse plane. With the blue curve representing the force response for a dimer in its standard orientation, orange being the inverted case, and green the same case but placed below the focus. . . . .	72
4.3 Equilibrium positions of optically trapped dimers with varying size ratio, dotted lines represent unstable traps whereas solid lines represent stable trapping positions. (a) shows that dimers with their smaller sphere orientated away from the focus have an expected single trapping position. (b) shows that when the same dimer is inverted $180^\circ$ there are now stable traps along the beam axis, one below the focus and one above the focus.	74
4.4 Trajectory map of simulations ran using a dimer of size ratio 2 with a laser power of 500 mW. The stable points are indicated by the larger spheres and the starting conditions are colour coded to match the stable point they end up in. Right hand render shows a dimer in its off-axis configuration . . . . .	75

## List of Figures

4.5	Rotation frequency vs component phase difference for differently sized dimers. The solid lines represent the rotation rate experienced while the dimer is in its standard orientation, whereas the solid points are for the case where the orientation is inverted. Laser power = 100 mW . . . . .	76
4.6	Rotation rate plotted against dimer size ratio for a variety of different simulation scenarios. The red line is for the case where the larger sphere is above the smaller sphere. The blue line is the inverted case, while the initial position is above the focus of the trap. And lastly the green line is again for the inverted case, but when the dimer's initial position is below the focus of the trap. . . . .	78
4.7	Optical torque against polar angle $\theta$ about the three primary axis (top: torque about the x-axis; middle: torque about the y-axis; bottom: torque about the z-axis) on a symmetric dimer in linear, elliptical, and circular polarisation beams. Diagram to the right is for visual clarity about the direction of $\theta$ . . . . .	80

## List of Figures

4.8 3 second trajectory of a dimer trapped in an off axis orientation, laser power was set to 100 mW. The far left column depicts the dimer's centre of mass position with time; middle two columns are the $x$ , $y$ , and $z$ components of the vectors $u_x$ and $u_y$ ; last column depicts the components of the vector $u_z$ which defines the dimer's orientation. . . . .	81
4.9 Rotational frequency vs laser power for a dimer in both vertical orientations. . . . .	82
4.10 Recorded power spectra fitted to eq. 2.45, scattered points represents the blocked data ( $n_b = 100$ ). Corner frequency for the Lorentzian curves are reported in the legend. . . . .	84

# List of Tables

3.1 Results from rotating vaterite within supersaturated solution of  $H_2O$  and Glycine. Solubility concentration for Glycine at 16° was  $C^* = 0.2016g/g$  65

# Preface/Acknowledgements

I would like to acknowledge...

## Chapter 0. Preface/Acknowledgements

# Chapter 1

## Introduction

Crystallisation is one of the oldest forms of phase separation used by humanity [3], put simply, it is the formation and growth of a new structured phase within a disordered bulk phase. This has applications in a number of industries such as pharmaceuticals, food production, and electronics [4]; where the extraction of dilute materials can help improve product quality while keeping production costs low. The industrialisation of crystallisation has allowed engineers to reliably and efficiently induce the crystal formation within a bulk phase. However, while on a large scale crystallisation is seemingly an understood physical process, just a small amount of investigation into the literature reveals that at a micro scale there is yet to be unifying theory that can accurately explain the process of crystallisation [5]. Of which there two primary areas of focus, nucleation and crystal growth. The latter focusing on how an already stable crystal grows and how it takes on its final shape; whereas the former is more concerned with which factors contribute to its formation in order to control crystal growth.

The focus of this research is partly based around investigating the impact of a

## Chapter 1. Introduction

focused electromagnetic field can influence the nucleation process by inducing shear flow within the bulk phase. This in hope that the localised EM field can be used to study different phenomena in nucleation in order to develop a better understanding of the underlying mechanisms.

### 1.1 Nucleation

Nucleation is an example of a binary phase separation, where a dilute phase is miscible in a bulk phase, more often called the solute and solvent respectively. Because of thermodynamics, the two can only remain in equilibrium while below a specific concentration ( $C_{eq}$ ) - below which the chemical potential  $\mu$  for a miscible solution is greater than the potential required to separate the two phases. Once  $C_{eq}$  is exceeded there is a chemical potential difference driving the solution to separate the two phases. Since different combinations of solute and solvent will have different equilibrium concentrations, researchers often instead measure the ratio between the solute and solvent by using 'supersaturation', one form of measuring supersaturation is shown below [6]:

$$S(T) = \frac{C_{sol}}{C_{eq}(T)} \quad (1.1)$$

Where  $C_{sol}$  is just the solute concentration,  $C_{eq}(T)$  is the equilibrium concentration at temperature  $T$ . While the solution remains supersaturated there is a chemical potential driving force for the solute to coalesce and separate from the solution as an ordered solid, the first formation of the crystal is referred to as the nucleus and understanding its formation has been the focus of researchers for decades now. Typically, for

## Chapter 1. Introduction

an industrial crystallisation process the working principle is based on controlling and manipulating the supersaturation of the system.

### 1.1.1 Primary vs Secondary nucleation

From an industrial perspective, the nucleation process can be broadly categorised into either primary or secondary nucleation. The former being described as the formation of an initial nucleus within the bulk phase; absent of any external stimuli primary nucleation is considered stochastic and is typically undesirable for industrial applications where short and consistent residence times are desirable. At a small scale one can estimate the nucleation rate by making repeated measurements of sample solutions and seeing how many have nucleated after a given time, giving us a Poisson distribution.

$$P(t) = 1 - \exp[-JV(t - t_g)] = \frac{M^*(t)}{M} \quad (1.2)$$

Where  $J$  is the nucleation rate,  $t_g$  is the 'growth time',  $V$  is the volume of the individual samples, and  $M^*(t)$  &  $M$  are the number of nucleated samples and the total number of samples used respectively. While this is useful for studying the effects of different parameters at a small scale, for industrial applications there are so many additional factors at play that can throw off this estimation.

In contrast, secondary nucleation is the result of a initial seed crystal inducing further nucleation within the bulk solution [7], in absence of a seed crystal nucleation is near impossible. The research of Secondary Nucleation is fascinating for its own merits;

is it speculated that the supersaturation barrier is non-existent [8], and furthermore there are a multitude of mechanisms that can induce secondary nucleation making it imperative that researchers can control the nucleation rate at an industrial scale.

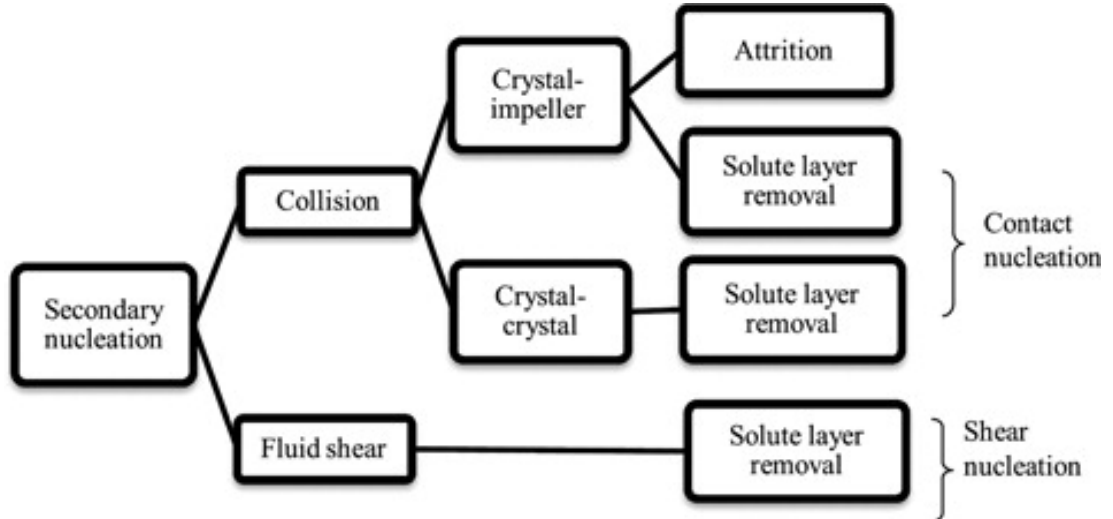


Figure 1.1: Secondary Nucleation mechanisms, classified by Agrawal and Paterson [1]

## 1.2 Nucleation Theories

### 1.2.1 Classical Nucleation Theory (CNT)

Sometimes referred to as 'Gibbs Nucleation Theory' the original theory was first formed from the works of Volmer and Weber, and Frenkel [9, 10]. While initially it was more focused into describing droplet formation in condensing vapours it was extrapolated to describe crystallisation. The central premise of classical theory is that nucleation occurs stochastically throughout the bulk phase due to collisions between individual solute molecules, ions, or atoms; at the same time the bulk phase is resistant to the formation of a new phase. The competition between these random collisions and the

## Chapter 1. Introduction

bulk solution can be used to predict the probability of a newly formed nucleus.

Consider a supersaturated solution, after some time enough individual sub units collide, forming a nucleus of volume  $4\pi r^3/3$ . The newly formed phase has a lower chemical potential than the surrounding solution, reducing the free energy of the system; at the same time, the formation of a new interface is resisted by the bulk phase due to surface tension. The net free energy of the system for a nucleus of radius  $r$  is given as [11]:

$$\Delta G = \frac{-4\pi r^3}{3v} k_B T \ln(S) + 4\pi r^2 \sigma_{inf} \quad (1.3)$$

Where  $v$  is the approximate volume of an individual molecule,  $k_B$  is the Boltzmann constant, and  $\sigma_{inf}$  is the interfacial tension of the bulk solution. Plotting the free energy of the system against nucleus size reveals a critical size above which the gain in free energy exceeds the interfacial tension.

The maximum value of  $\Delta G_{tot}$  is the free energy barrier that any newly formed nucleus needs to overcome in order to stabilise. The nucleation rate (the volume of new crystalline material formed per unit time), is therefore commonly defined as being dependent on the energy barrier  $\Delta G^*$ :

$$J = A \exp \left[ -\frac{\Delta G^*}{k_B T} \right] \quad (1.4)$$

Where  $A$  is a pre-factor that can be fine tuned to the exact demands of the system (typically involving Zeldovich Factor,  $Z$ ) the free energy barrier can be found by finding

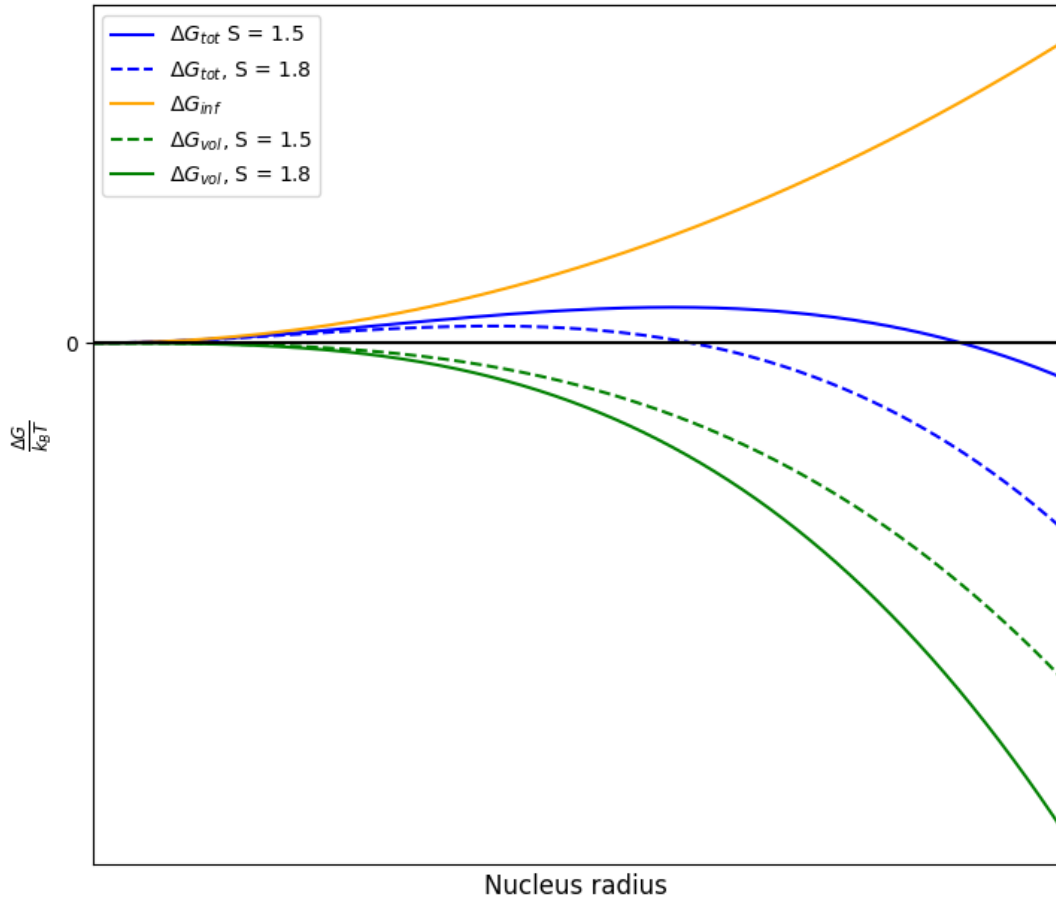


Figure 1.2: Free energy diagram of a newly formed nucleus according to the Classical Nucleation Theory. The total free energy (blue) is due to the competition between the volume free energy gain (green) and the interfacial free energy cost (orange). Dotted lines are for a higher supersaturation than the solid lines, the interfacial energy cost is independent of supersaturation.

the turning point of  $\Delta G_{tot}$ .

So to find the critical size  $n^*$  - and therefore the nucleation rate - we simply need to know the ratio between the interfacial free energy and the volume free energy. The CNT assumes that the crystal grows is purely spherical and that the interfacial free energy is near constant (aka that of a flat surface), this assumption is not very accurate for small crystal nucleus where the changing curvature means that the surface tension

## Chapter 1. Introduction

varies as a function of the crystal radius. This also assumes the surrounding fluid is at rest and there are no external forces on the nucleus that might distort the shape of said nucleus; though there has been theoretical work looking into how the CNT behaves under shear flow [12–14]

Furthermore, multiple experiments have already verified that crystals can form any number of structures and can even transition through multiple structures as it grows, meaning that the interfacial tension will constantly change as the particle grows. Furthermore, because we are assuming that the surface energy is constant the pre-exponential factor that is computed from experimental data, and the factor predicted by theory often disagree with one another to several degrees of magnitude.

There are several results that indicate that the CNT is not a good fit for nucleation rates:

- Discrepancy in vapor-liquid nucleation systems to the extent that CNT was off by a factor of more than 2000 [?]
- In glass formation, nucleation kinetics are incredibly important to understand as the crystallization process is not desired when producing glass. We want to cool the molten solution so that the solid does not have time to reorganize itself into an ordered structure. To understand nucleation kinetics in glass formation we need to understand that as crystals form in the glass the surface energy differs from the stable phase significantly which us poorly predicted by CNT as it assumes that crystals will have a constant structure and interaction with the bulk material [ ].
- Metal alloys can demonstrate super-cooling while not experiencing nucleation,

this is because in these liquids exhibit short range dynamics which means that the liquid droplet remains unordered as it is cooled. Because CNT assumes that the droplets must be of a similar ordering to that of the bulk crystal it often struggles to consider systems where the local bond order can fluctuate between phases. [ ]

CNT is often regarded as a good description of the macro system, its obvious that for all crystallization systems there is an inherent energy barrier that dictates the nucleation rate. However, for such a diverse range of possible nucleation events the CNT crudely assumes all interactions between solutes as identical; this makes it difficult to model crystallisation events using CNT without significantly modifying the model for each specific case. Recent developments in studying nucleation events have opened up new possible 'pathways' for a nucleation event to go down, by far the most common is the idea of Two step nucleation.

### 1.2.2 Two Step Nucleation

The two step nucleation theory is an extension to the CNT, colloid simulations showed that short range (such as in proteins [15, 16]) interactions allow for the formation of a liquid-liquid metastable phase from which a new solid phase could form [11, 17]. *in situ* techniques for studying nucleation several papers reported the presence of stable liquid-like clusters that formed prior to nucleation [15, 18, 19]. It can be understood by Oswald's rule [20], which says that any crystallising system does not take the path to the lowest possible energy state but instead first transitions to the state with the smallest free energy barrier, further transitions can still occur but this method minimises the

## Chapter 1. Introduction

overall free energy cost. If we consider the free energy diagram from before (fig. ??) we can consider a case where the supersaturation is low ( $S \approx 1.01$ ) then a dense liquid droplet will have a lower chemical potential than the surrounding fluid

### 1.3 Crystallisation methods

#### 1.3.1 Cooling Crystallisation

For some binary mixtures the supersaturation is heavily dependent on the solution temperature, therefore a simple method of producing crystals is by cooling the mixture to induce crystal formation. At ambient temperatures the solute concentration is too high to be fully incorporated into the solution ( $S \gg 1$ ), after heating however the solute is fully dissolved into the solution ( $S < 1$ ). Now as the mixture is allowed to cool to room temperature the supersaturation will increase until crystal formation begins, the rate of cooling drastically influencing the size and number of crystals produced.

If  $dT/dt$  is high then the final product will consist of large crystal and be low in number, as the nucleation rate is directly related to the supersaturation only a handful of nuclei can form before the remaining solute grows onto the surface. If  $dT/dt$  is low then the final product will consist of smaller crystals and be far more numerous, as the supersaturation is so large that the new nuclei are forming continuously. Between these two extremes, one can define the meta-stable zone width, a region in the temperature-concentration phase space where both nucleation and crystal growth can be reliably controlled. The lower limit being given by the solubility curve of the binary mixture, and the upper limit being defined by the metastable zone.

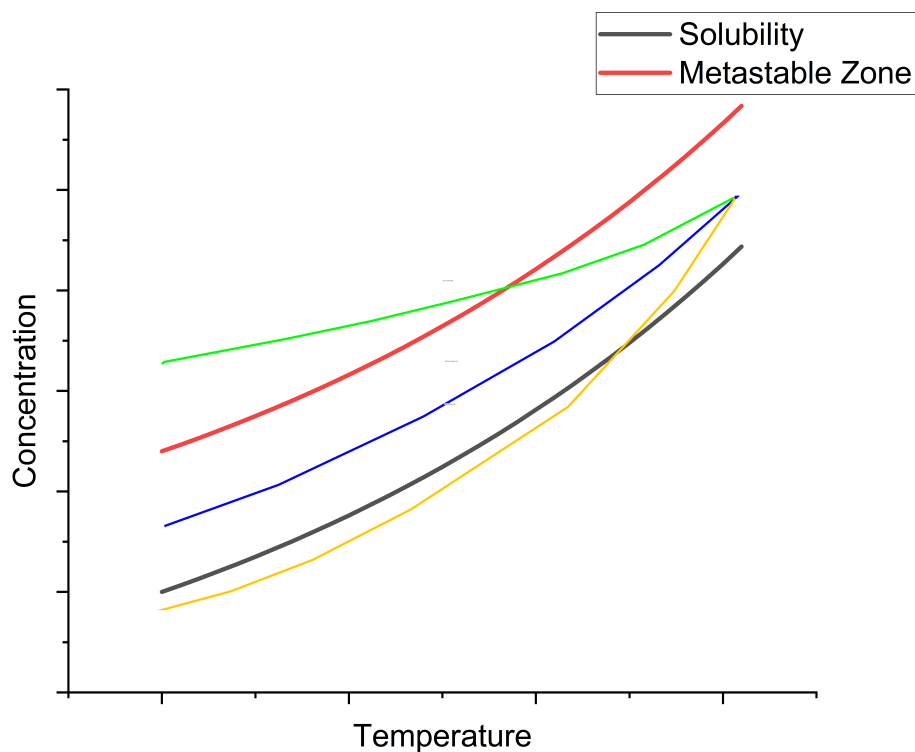


Figure 1.3: Typical Concentration vs Temperature plot with the solubility curve (black) and metastable zone (red). 3 different cooling curves are shown as well: a high rate of cooling (orange) shows the mixture quickly dropping below the solubility curve resulting in no new nuclei forming; a low rate of cooling (green) shows the mixture exceeding the metastable zone, where now nucleation occurs freely; and a typical cooling rate (blue) shows how a typical cooling crystalliser will operate, sitting in the middle of the other two curves.

The viability of cooling crystallisation is dependent on the meta-stable zone width, too narrow and the process is difficult to control, too wide and the crystal growth rate may be insufficient for the desired outcome.

## 1.4 Optical Tweezers

### 1.4.1 Background

Optical tweezing has been a field of applied optics ever since the 1970s when Ashkin [21] first showed that focused light was capable of exerting 'radiation pressure'. The working principle was that a light source such as a laser could trap small objects within a 2D plane, as long as the light source had a symmetrical profile and whose intensity was concentrated around a central axis. Soon after, Ashkin showed that the introduction of a microscope objective would allow one to focus the light source to a diffraction limited point that would stably trap small objects within a confined volume [22]. This allowed Ashkin and others to study biological material and would later be used to probe microscopic properties such as the formation of colloidal aggregates [23] to the drag forces exerted by a pure vacuum [24, 25]. Due to the predictable behaviour of light, optical tweezers have become essential for measuring and exerting precise forces on the magnitude of pico-newtons allowing one to probe the material properties of the smallest materials.

### 1.4.2 Literature related to laser induced nucleation

From as early as 1996 it has been known that laser irradiation is a viable method of inducing nucleation within a supersaturated solution [26], the first reported case was notable as it used a  $1.064 \mu m$  laser meaning it was unlikely to be a photo-chemical reaction but rather a physical one. Future research has found nucleation can be induced by 1 of 3 routes involving direct laser induction: firstly, Non-photochemical laser induced

## Chapter 1. Introduction

nucleation (NPLIN) where the solution is irradiated with a pulsed laser [26–28], several papers have debated the exact mechanism that induces NPLIN [27, 29]. Two suggested hypothesis are: an optical Kerr effect, where the solute molecules are aligned to lower the nucleation barrier [29]; a dielectric polarisation effect, in which solute clusters are stabilised within the electric field which drastically increases the likelihood of nucleation [30]. Both hypothesise have their limitations and there has yet to be a single theory that explains NLPIN thoroughly. In either case the mean pulse intensity needs to be kept relatively low (on the order of  $0.1 - 0.01\text{GW}/\text{cm}^2$ ), as high intensity pulses lead to a completely different nucleation mechanism.

High intensity laser induced nucleation (HILIN), where the pulse intensity is on the order of several  $\text{PW}/\text{cm}^2$  is far simpler a mechanism to explain in comparison to NPLIN. The production of nuclei can be wholly associated to a cavitation process within the target solution, where the laser focus results in thermo-cavitation and the subsequent pressure change leads to a nucleation event around the focus of the laser [ , , ]. There is still not a general consensus on how cavitation influences the local supersaturation [ , ], nor is there a clear understanding of what properties of the crystal can be controlled [ , ]. It has been suggested that in theory any solution can undergo HILIN [ ], proving such a theory requires a strong understanding of the phenomena both before and after cavitation occurs.

Lastly, there is trapping induced nucleation, this is where optical tweezers come into play, the optical trap has been shown to have different effects on supersaturated solutions depending on where it has been focused. When focusing on the cover slip, supersaturated solutions of glycine and  $D_2O$  were shown to create a dense liquid droplet

## Chapter 1. Introduction

of glycine and water [ , ], applying DLS analysis showed that the dense liquid region was populated by clusters that would consolidate together upon being focused by the optical trap [ ]. Molecular simulations of glycine solutions showed that these clusters are unstable when using pure glycine below the saturation point [ ] suggesting that the clusters are formed due to glycine reaction products. When the optical trap was moved from the cover slip to the air-solution interface nucleation would occur before a dense liquid region could form [ ]. Repeated experiments where the laser is focused on the air-solution interface have lead to a variety of different nucleation events. In some instances the nucleation occurs spontaneously after a short period of time [ ]; whereas allowing a solution to age results in the formation of amorphous precursors that when irradiated will nucleate immediately [ ]. The precursors are only seen when the solution is irradiated by an optical tweezer and the growth rate can be controlled somewhat by varying the laser power [ ]. Notably the only work has been done with simply irradiating the solution with a trapping potential, there has not been an attempt to introduce a trappable object into the solution, the trapping potential has been used to influence the growth of a crystal front [ ].

### 1.4.3 Optical Rotation

For any electromagnetic field it is possible to transfer both linear and angular momentum [ ]; more accurately the field is said to have both orbital and spin momentum. Though there is some debate on how to decompose the total momentum into these two components [ ], for this thesis we do not need to calculate the exact quantities and will instead look at the broader effects of both components. The orbital momentum

## Chapter 1. Introduction

can be understood as the shape of the wavefront of the particular field in question, for simple Gaussian beams the wavefronts are uniform and equally spaced resulting in the typical radiation pressure that Ashkin and co demonstrated [ ]. However, higher order modes of a Gaussian beam (such as the Laguerre-Gaussian modes) have non-uniform wave fronts meaning the orbital momentum has both angular and linear components; depending on the relative size of the target particle one can induce rotation, or orbiting [ ]. Spin angular momentum (SAM) is attributed to the spin density of the field, early research has shown that the spin density is non-zero for any beam but while the SAM can easily be zero for homogeneous scatterers, this has sparked debate if SAM is even a physical quantity as it does not aid in the transport of energy directly [ ]. This paradox is resolved by representing the wave as an array of finite loops that all together cancel one-another out when the medium is homogeneous, when inhomogeneity is introduced (such as by being refracted by a birefringent medium) these circular loops no longer cancel out resulting in a non-zero SAM [ ], depending on the material a number of rotational effects can occur.

For a perfectly homogeneous non-absorbing sphere the total SAM transferred from a circularly polarised beam is zero; if, however, the wave front of the beam is helical - for example using a Laguerre-Gaussian beam [ ] - one can control the rotational motion via transfer of OAM. Due to the structure of the LG beam the individual rays are not perpendicular with the propagation direction; as a trapped particle will experience a constant torque while being pulled towards the centre of the trap focus. This was demonstrated in [ ] where Copper Oxide micro particles rotated with a frequency of around 2 Hz due to the orbital AM from a LG beam; this was enhanced further

## Chapter 1. Introduction

by circularly polarising the trapping beam. Typically for a non-absorbing particle the polarization state of the beam has a negligible impact on the angular momentum transferred, this is not the case for particles with a high absorption efficiency as the combined handedness of the LG beam and polarisation vector can lead to an enhanced transfer of SAM. However, by far the best method for inducing rotation is using birefringent materials.

Birefringence is a material property often seen in crystalline materials, if the crystal lattice has a different structures when viewed at different orientations then light will be refracted differently depending on its polarisation. For circularly polarised light the inhomogeneity results in a high degree of SAM being transferred to the target object [ ], this has been exploited to rotate microspheres as fast as 1000 Hz while suspended in a bulk medium [ ] as well as a means of measuring the local temperature and shear response of said medium [ , ]. Calculating the optical torque applied to a birefringent material is given via:

$$\begin{aligned}\tau_{opt} = & -\frac{\epsilon}{2\omega_{laser}} E_0^2 \sin(kd(\Delta n)) \cos 2\theta \sin 2\phi \\ & + \frac{\epsilon}{2\omega_{laser}} E_0^2 (1 - \cos(kd(\Delta n)) \sin 2\phi)\end{aligned}\quad (1.5)$$

Where  $\theta$  is the angle between the particle's orientation vector and the propagation direction of the EM field, and  $\phi$  is the phase shift in the EM field. The first term represents the 'orientational' torque which is due to the target particle being aligned along the EM field, when aligned  $\theta = 0$  meaning the entire term is negligible for particle's with a stable orientation. The second term is due purely to the polarisation of the optical trap, for circularly polarised light  $\phi = \pi/4$  thus maximising the torque

## Chapter 1. Introduction

transferred to the target particle. Birefringence can also be induced if the target particle has an anisotropic shape, in particular if the particle shape is elongated along one major axis; the go to particle shape is a silica dimer (two spheres tangentially attached) due to silica's stability and strong adhesion. Using a silica dimer research groups have achieved a rotation frequency in the realm of several GHz [ ] in a vacuum.

### 1.4.4 Shear induced Nucleation

It has long been known that solution nucleation is influenced by shearing of the fluid, from stirring agents in the container (i.e. propellers) to the container boundary layers, however there has yet to be a clear mechanism by which said shearing effects the nucleation event. Theoretical research into shear induced nucleation suggests that there should be a slight increase in the nucleation rate at low shear rates, reaching a maximum increase in nucleation rate, and then at higher shear rates the nucleation rate begins to drop off. This has been shown theoretically for both simple colloidal [12–14] and ice crystal formation [31]; however, no experimental work into these systems has been conducted to prove this is the case. There is some experimental evidence for this phenomena in simple salt and protein solutions - though the authors emphasise that mechanical agitation cannot be ruled out - there has not been a exhaustive study into the shearing effects apart from in glycine solutions. In [12] it was found that a shear rate of around  $3000\text{ s}^{-1}$  was the maximum shear rate that would yield the highest nucleation rate. Using the theoretical model established in [13, 32] which modifies the CNT to account for the effects of a nucleus undergoing shearing, accounting for the fact that a nucleus' growth is undergoing competition between flow-mediated molecular transport

## Chapter 1. Introduction

and the strain applied by the flow field which inhibits the growth of the nucleus. There central conclusion (from both the theoretical and experimental results) is that there is an optimal shear rate in which the nucleation rate is maximised. However, a question that arises from this result, if there is a optimal shear rate in which molecular transport is maximised and strain is minimised, then surely there should also be a shear rate in which the molecular transport and strain are equal - allowing one to suspend a nucleus at a constant radius. In this scenario, the molecular transport would prevent the nucleus from dissolving, but the strain would prevent the nucleus from growing. This however would require one to be able to apply a continuous shear rate to a targeted nucleus with high precision, there is also no model for an individual nucleus undergoing growth.

## 1.5 Aims and Objectives

Overall the aim of the PhD is to study viability of using micro-rotors to generate localised fluid flow around the beam focus. The results are reported in chapter 3, this is then succeeded by experimental work where we instead using a galvano-mirror to generate a moving beam focus within an undersaturated solution to control the crystal growth front. In addition, computer simulations into asymmetric dimers and their applications as complex micro-rotors are discussed in chapter 4. Lastly two novel methods of measuring rotational motion are discussed in chapter 5; firstly via a novel detection fibre method that allows for instantaneous measurements of the orientational behaviour of optically trapped ellipsoids/dimers; and secondly we create a simulative quadrant photo diode that replicates laboratory results, utilising linear regression techniques we

## Chapter 1. Introduction

measure the change in orientation in order to measure the optical torque applied to a non-birefringent particle.

# Chapter 2

## Theory and methods

The two key areas of this project cover two widely different fields; crystallisation theory, which is covered in the previous introduction section, and tweezing theory. The following chapter summarises the working principles behind optical tweezing, the work being done with optical tweezers in particle classification, and how tweezing has been used to investigate nucleation events.

### 2.1 Working Principle

Optical tweezing operates on the principle that light carries both linear and angular momentum, which can be transferred to other objects. If light is reflected or refracted by a medium part of the light's momentum is transferred to the medium itself. While at large scales this effect is insignificant in most cases, at micron scales the forces imparted by individual photons begin to become significant enough to influence its trajectory. Ashkin's work into optical tweezing found that micron sized entities could be spatially locked by aiming a laser with a Gaussian intensity profile directly upward at a the cell

## Chapter 2. Theory and methods

while being suspended in a liquid medium [21]. This is demonstrated diagram below where we have a simple sphere trapped by a Gaussian beam, if we consider two rays of light hitting our sphere we see that while in the centre each ray is refracted in an equal opposite direction to one another and so the net force imparted is 0. However when displaced the net force is unbalanced and points towards the centre of the trap; this principle can be generalised to 3 degrees of freedom if we consider a focused beam instead of a para-axial beam, typically the trap will be weaker along the beam axis compared to the transverse trap strength.

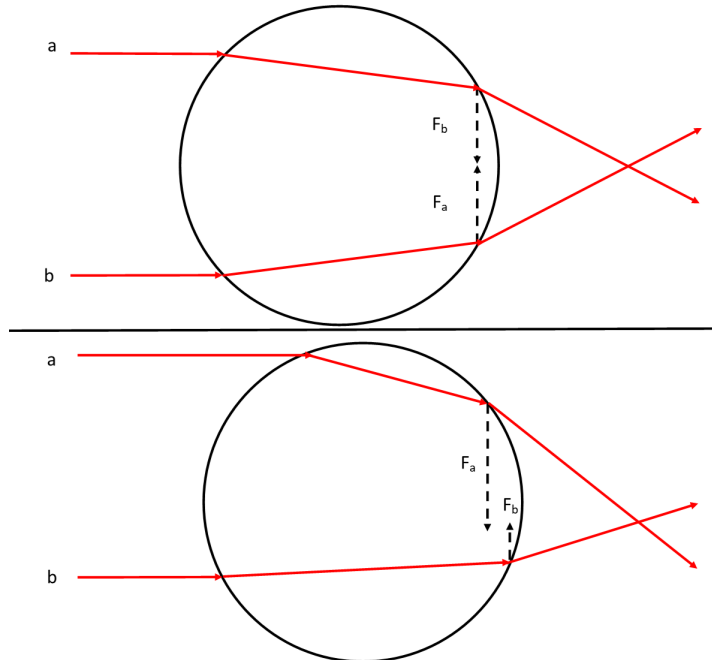


Figure 2.1: Working principle for an optical trap, upper image shows a sphere at the centre of a trap experiences equal forces directed towards inwards. Lower image shows that when displaced 'ray a' is refracted far more than 'ray b' resulting in a net force back towards the centre.

## 2.2 Electromagnetism and optical tweezing

Proper understanding of optical tweezing requires an understanding of how the trapped particle interacts with the trapping laser. From a electromagnetism perspective the laser creates a spatially and temporally coherent electric field that scatters light off of a trapped particle. The laws governing electric and magnetic fields are summarised most succinctly via the Maxwell equations. The differential forms of which are given below [33]:

$$\nabla \cdot \mathbf{E} = \frac{\rho_v}{\epsilon_0} \quad (2.1)$$

$$\nabla \cdot \mathbf{B} = 0 \quad (2.2)$$

$$\nabla \times \mathbf{E} = \frac{\partial \mathbf{B}}{\partial t} \quad (2.3)$$

$$\nabla \times \mathbf{B} = \mathbf{j} + \frac{\partial \mathbf{E}}{\partial t} \quad (2.4)$$

where  $\rho_v$  is the free charge density,  $\mathbf{j}_0$  is the charge current, and  $\epsilon_0$  is the permittivity of free space.

These 4 equations describe how the electric and magnetic fields behave and are related to one another at a microscopic level. Any discussion of optical trapping is underpinned by the fact that in all cases the Maxwell Equations must be satisfied at the macroscopic level, where one must account for the medium's interactions with the

## Chapter 2. Theory and methods

EM field. Macroscopic forms of the maxwell equations are given below [33]:

$$\nabla \cdot \mathbf{D} = \rho_f \quad (2.5)$$

$$\nabla \cdot \mathbf{B} = 0 \quad (2.6)$$

$$\nabla \times \mathbf{E} = \frac{\partial \mathbf{B}}{\partial t} \quad (2.7)$$

$$\nabla \times \mathbf{H} = \mathbf{J}_f + \frac{\partial \mathbf{D}}{\partial t} \quad (2.8)$$

Where  $\rho_f$  and  $\mathbf{J}_f$  are the charge density and current caused by the presence of free charges in the medium, and  $\mathbf{D}$  and  $\mathbf{H}$  are the displacement and magnetizing fields respectively. The latter two are defined by:

$$\mathbf{D} = \epsilon_0 \mathbf{E} + \mathbf{P}$$

$$\mathbf{H} = \frac{1}{\mu_0} \mathbf{B} - \mathbf{M}$$

Where  $\mathbf{P}$  is the polarization field and  $\mathbf{M}$  is the magnetisation field, these fields arise due to the bound charges throughout the medium interacting with the EM field.

The force exerted by an optical tweezer can be subdivided into the gradient and scattering components, for most modelling research this is how the force fields are reported. The gradient force is a conservative force brought about by the polarisation of dielectric materials, anything around 10% of the trapping wavelength will be attracted along the gradient of the electric field to the region of greatest intensity (for a simple Gaussian Beam this would be at the focal point). The scattering force arises from the scattered field of the trapping beam pushing the target object away from the focal

## Chapter 2. Theory and methods

point; unlike the gradient

force, the scattering force is non-conservative and is loosely proportional to the particle's Brownian motion. The equilibrium position (where the mean squared displacement is minimised) is found when the gradient force far exceeds the scattering force, interpreting and calculating these forces is dependent on the ratio between the particle size and the trapping wavelength.

### 2.2.1 Ray-Optics Regime

The Ray-Optics model is the simplest to understand, the theory models the laser as a collection of individual 'rays' that propagate and are refracted according to Snell's Law. Based on the change in direction momentum is transferred to the target particle; with rays closest to the centre of the beam having greater intensity than those rays at the very edge of the beam. Consider a particle struck by two rays in a Gaussian beam (see Fig below), one coming close to the centre, and the other ray coming from the edge. As each ray is refracted by the target sphere a force is imparted onto it, the total force imparted is given by:

$$F_i = Q_i \frac{\Delta n P_i}{c} \quad (2.9)$$

where  $Q_i$  is the trapping efficiency,  $\Delta n$  is the difference in refractive indices between the solution and the target particle, and  $P_i$  is the power of the individual ray. For a beam with a Gaussian intensity distribution  $P_i$  will fall off as you move from the centre of the beam. The ray optics model is ideal for

### 2.2.2 Lorenz-Mie Theory

The Lorenz Mie theory provides an exact solution to the maxwell equations for the scattering caused by an isotropic sphere. The theory describes the scattered wave given off by a dielectric sphere when incident by a plane wave as a summation of partial spherical waves. For any spherical wave the vector fields must solve the Helmholtz wave equation given by:

$$\nabla^2 \mathbf{E} + k^2 \mathbf{E} = 0 \quad (2.10)$$

Where  $k$  is the wave number of the electromagnetic radiation ( $k = 2\pi/\lambda$ ) This combined with the constraints of Maxwell's Equations leaves very few exact solutions apart from spherical or planar waves, both of which can be converted between with relative ease. For example, a plane wave electric field can be expanded into spherical harmonics and likewise any spherical wave can be described as combination of plane waves offset from one another. For a single plane wave the incident, internal, and

## Chapter 2. Theory and methods

scattered fields are given as:

$$\mathbf{E}_{\text{inc}}(\mathbf{r}) = E_0 \sum_{nm}^{\infty} \left[ a_{nm} \mathbf{M}_{nm}^{(1)}(\mathbf{r}) + b_{nm} \mathbf{N}_{nm}^{(1)}(\mathbf{r}) \right] \quad (2.11)$$

$$\mathbf{E}_{\text{int}}(\mathbf{r}) = E_0 \sum_{n=1}^{\infty} i^n \frac{2n+1}{n(n+1)} \left[ -id_{nm} \mathbf{N}_{nm}^{(1)}(\mathbf{r}) + c_{nm} \mathbf{M}_{nm}^{(1)}(\mathbf{r}) \right] \quad (2.12)$$

$$\mathbf{E}_{\text{scat}}(\mathbf{r}) = E_0 \sum_{n=1}^{\infty} i^n \frac{2n+1}{n(n+1)} \left[ -ip_{nm} \mathbf{N}_{nm}^{(3)}(\mathbf{r}) + q_{nm} \mathbf{M}_{nm}^{(3)}(\mathbf{r}) \right] \quad (2.13)$$

$$\mathbf{E}_{\text{tot}}(\mathbf{r}) = \begin{cases} \mathbf{E}_{\text{inc}}(\mathbf{r}) + \mathbf{E}_{\text{scat}}(\mathbf{r}) & \text{if } \mathbf{r} \text{ outside} \\ \mathbf{E}_{\text{int}}(\mathbf{r}) & \text{if } \mathbf{r} \text{ inside} \end{cases} \quad (2.14)$$

where  $a_{nm}$ ,  $b_{nm}$ ,  $c_{nm}$ ,  $d_{nm}$ ,  $p_{nm}$ , and  $q_{nm}$  are the expansion coefficients of each of the fields, and  $M_{nm}^{(1)}$  and  $N_{nm}^{(1)}$  are the vector spherical harmonics. For the incident field computing its expansion coefficients is possible via analytical methods and are completely dependent on the beam conditions imposed by the user. However, computing the expansion coefficients of the internal and external fields be far more tedious depending on the shape of the target and what properties of the scattered field are desired — all of which is discussed later on. From an optical trapping perspective the force exerted by a focused electric field can be found by computing the Maxwell stress tensor which only requires the total magnitude of the incident and scattered fields, essentially computing the momentum contained in the incident beam and how much of it has been transferred to the target particle.

Lorenz-Mie theory can be applied to describe the scattering from any particle regardless of size, however as we either increase or decrease the size of the target particles the infinite series converges allowing one to ignore much of the tedium of Lorenz-Mie

## Chapter 2. Theory and methods

theory. The ray optics model is what is achieved when the size of the target particle far exceeds that of the laser wavelength and thus individual ray's can have independent contributions. In the latter case we can simplify the scattering problem by approximating our target as a single dipole, focusing only its interactions with the incident field.

### 2.2.3 Rayleigh Regime

The Rayleigh approximation is the limiting approximation for describing a particles motion in an electromagnetic field who's wavelength is several times greater than the particle's size. The underlying theory is that a dielectric sphere can be treated as a dipole while in the presence of the electromagnetic field; in which case the scattering force is given simply by the scattering of the induced dipole, and the gradient force is due to the Lorentz force [34]. The gradient forces in the principle Cartesian axis are described by Harada et al [35] in MKS units as a restorative rectangular force field:

$$F_{grad,x} = -\hat{x} \frac{2\pi n_2 a^3}{c} \left( \frac{m^2 - 1}{m^2 + 2} \right) \frac{4\tilde{x}/w_0}{1 + (2\tilde{z})^2} \times I(r) \quad (2.15)$$

$$F_{grad,y} = -\hat{y} \frac{2\pi n_2 a^3}{c} \left( \frac{m^2 - 1}{m^2 + 2} \right) \frac{4\tilde{y}/w_0}{1 + (2\tilde{z})^2} \times I(r) \quad (2.16)$$

$$\begin{aligned} F_{grad,z} = -\hat{z} \frac{2\pi n_2 a^3}{c} \left( \frac{m^2 - 1}{m^2 + 2} \right) \frac{4\tilde{z}/w_0}{1 + (2\tilde{z})^2} \times I(r) \\ \times \left[ 1 - \frac{2(\tilde{x}^2 + \tilde{y}^2)}{1 + (2\tilde{z})^2} \right] \end{aligned} \quad (2.17)$$

where:

$$I(r) = \left( \frac{2P}{\pi w_0^2} \right) \frac{1}{1 + (2\tilde{z})^2} \exp \left[ -\frac{2(\tilde{x}^2 + \tilde{y}^2)}{1 + (2\tilde{z})^2} \right] \quad (2.18)$$

## Chapter 2. Theory and methods

Where  $m$  is the relative refractive index ( $n_1/n_2$ ),  $\omega_0$  is the beam waist, and  $a$  is the radius of the particle. Scattering force however is dependent on the effective scattering cross sectional area.

$$F_{\text{scat}} = \hat{z} \left( \frac{n_2}{2} \right) C_{pr} I(r) \quad (2.19)$$

where:

$$C_{pr} = \frac{8}{3} \pi (ka)^4 a^2 \left( \frac{m^2 - 1}{m^2 + 2} \right)^2 \quad (2.20)$$

The Rayleigh regime allows for easy computation of the gradient and scattering forces due to the assumption that the particle is a point dipole, so much so that higher order scattering problems can be simplified by subdividing the particle into discrete dipoles (see Sec 2.3). However as the target particle gets larger this assumption fails to accurately describe the trapping force due to the complexity in the gradient field. For particle sizes close to the laser wavelength the scattered field is best described by Lorenz-Mie theory.

### 2.3 Scattering methods

There are several methods available to calculate the scattered field produced by a particle, while one can compute this from directly applying Lorenz-Mie theory for complicated particle shapes and focused beams makes it tedious for some applications.

### 2.3.1 T-matrix Method

The  $T$ -matrix method was first developed by Peter Waterman with his research into acoustic wave scattering [36], this would later be extended to electromagnetic waves. Sometimes being referred to as the extended boundary condition method (ECBM), the method replaces the scatterer with a series of surface currents over the targets surface, these currents are chosen so that the electric field outside is identical to the original problem [37]. This choice of currents negates the need to compute the internal fields which reduces the scattering problem to a system of linear equations relating the incident beam coefficients to the scattered beam coefficients the relationship between each can be summarised as:

$$\begin{pmatrix} q_{mn} \\ p_{mn} \end{pmatrix} = \mathbf{T} \begin{pmatrix} a_{mn} \\ b_{mn} \end{pmatrix} = \begin{pmatrix} T_{11} & T_{12} \\ T_{21} & T_{22} \end{pmatrix} \begin{pmatrix} a_{mn} \\ b_{mn} \end{pmatrix} \quad (2.21)$$

Where  $q_{mn}$ , and  $p_{mn}$  are the scattering beam coefficients, and  $a_{mn}$ , and  $b_{mn}$  are the coefficients of the incident beam. For this PhD in particular we utilise an extension of the ECBM known as multi-sphere  $T$ -matrix method (*mstm*), developed by Mackowski [38] the computational code computes the scattered field from each sphere within the target cluster and the incident field itself, this scattering between spheres converges to a final result but modern codes truncate the calculations to fit a desired accuracy and computational time.

The  $T$ -matrix method is exceptionally useful for computing the scattering from any arbitrary spherical aggregate. However, the  $T$ -matrix method by itself can be

## Chapter 2. Theory and methods

computationally taxing as the number of spheres increases [38]. While it is possible to solve for the scattering of each individual sphere this is only applicable for a single orientation and can be even slower for large aggregates [39,40]. The benefit of *mstm* is that the major scattering properties (scattering and extinction cross sections, scattering matrices, etc) can all be computed both for single orientations, or averaged over multiple orientations to determine the average scattering from the target particle.

### 2.3.2 Discrete Dipole Approximation

The discrete dipole approximation (DDA) is a general method that can be applied to the scattering from particles of arbitrary composition and geometry. Developed by Purcell and Pennypacker [41], the DDA method approximates the particle as being constructed of dipoles. Each dipole interacts with both the incident field and the scattered fields from every other dipole surrounding it. The resulting scattered field is identical to the scattered field produced by direct integration of Eq. 2.12 throughout the full particle volume [42]. The integral form for the internal electric field inside a scatterer is given as:

$$\mathbf{E}(\mathbf{r}) = \mathbf{E}_{\text{inc}}(\mathbf{r}) + \int_{V/V_0} d^3r' \bar{\mathbf{G}}(\mathbf{r}, \mathbf{r}') \chi(\mathbf{r}') \mathbf{E}(\mathbf{r}') \quad (2.22)$$

Where  $\bar{\mathbf{G}}$  is the Greens dyadic function of free space, which defines the impulse response between two separate dipoles; and  $\chi$  is the susceptibility of the medium, which describes the degree of polarisation of the medium in the presence of an electric field. With the internal field calculated the scattered field can be computed, one of the

## Chapter 2. Theory and methods

primary advantages of DDA over the T-matrix method is that the the composition of the target can be changed freely. When comparing different computational scattering methods, the ECBM was found to be better suited for simulating the scattering of symmetric targets as the ECBM can use the targets symmetry to speed up calculations [37], however when dealing with inhomogeneous media DDA is more efficient compared to ECBM.

### 2.4 Langevin Equation

Describing any microscopic motion requires an understanding of a molecules diffusive behaviour, for the case of optical tweezers the most complete model of diffusion is the Langevin equation. Models such as the Fickian, and Einstein derivations are sufficient for macroscopic behaviours the Langevin equation better describes the microscopic characteristics of any diffusive behaviour. The Fickian model is not suitable for the applications of optical tweezers as it assumes that all diffusive motion is driven by a gradient of molecular density [43], not only is this often not the case but it fails to describe the motion of any single molecule, only the collective behaviour. Einstein's model however considers the collisions experienced by individual molecules [44], if we assume that all collisions are random and only consider the behaviour after a finite time step  $\delta t$  then the individual collisions should cancel out, of course trying to understand the dynamics over a shorter period of time is not described by Einstein's model as you would have to consider each collision in turn [43, 43]. This is insufficient for our interests as an optical tweezers relaxation time (given by  $\tau = \kappa/\gamma$ ) is often so short

## Chapter 2. Theory and methods

that we must consider the individual collisions experienced by any one molecule. The Langevin model of diffusion therefore assumes that the net force on a particular particle is described fully by these individual collisions [45]:

$$m \frac{dv}{dt} + \gamma_0 v + F(t) = W(t) \quad (2.23)$$

Where the first term accounts for inertial forces, the second term accounts for friction forces which counteract the particles current motion ( $\gamma_0$  is the friction coefficient), and the final term accounts for the random Brownian force. The  $F(t)$  is there for convention which accounts for any external forces acting on the particle. We can say that the noise term  $W(t)$  has a Gaussian probability, with a correlation function of:

$$W(t) = \sqrt{2k_B T \gamma_0} \eta(t) \quad (2.24)$$

$$\langle W_i(t) W_j(t') \rangle = 2k_B T \gamma_0 \delta(t - t') \quad (2.25)$$

The Langevin model can be extrapolated to describe the diffusive behaviour of an overall system, but for this project we can instead consider the behaviour of some particle with a diffusion tensor  $D$  suspended in a viscous fluid and spacially localised by an optical potential with trap strength  $\kappa$ . Assuming the only external force acting on our particle is the laser the net force should be exactly equal to force of the stochastic collisions due to the fluids thermal energy. If we focus our analysis when the particle is stably trapped and assume that the trap is harmonic we can model the trapping force as a Hookean spring ( $F(t) \approx \kappa x(t)$ ). The full Langevin equation for an optically

## Chapter 2. Theory and methods

trapped particle is therefore given as:

$$m \frac{\delta^2 x(t)}{\delta t^2} + \gamma_0 \frac{\delta x(t)}{\delta t} + \kappa_x x(t) = \sqrt{2k_B T} \eta(t) \quad (2.26)$$

Eq. 2.26 provides an accurate description of strongly trapped particles, however the analytical solution of the Langevin equation requires integration of the white noise term making it difficult to simulate the trajectory of a given particle [46]. Instead it is often far easier to solve the equation numerically and apply use the analytical solution to calibrate and extract information about the particle and fluid, and how the two interact with the optical trap.

### 2.4.1 Finite Difference

The Finite Difference approach involves discretizing the time and spatial elements in order to approximate the higher order terms. If we assume that  $x(t)$  is differentiable to n (we can find its  $n^{th}$  derivative) then we can use the Taylor series expansion to get:

$$x(t + \Delta t) = x(t) + \frac{x'(t)}{1!} \Delta t + \frac{x''(t)}{2!} \Delta t^2 + \dots + \frac{x^n(t)}{n!} \Delta t^n + R_n(x(t)) \quad (2.27)$$

Where  $R_n(x(t))$  is the remainder term between the Taylor expansion to term n and the actual expression. If we limit our approach to the first derivative only we find that for

## Chapter 2. Theory and methods

sufficiently small values of  $R_1$  the velocity and acceleration can be approximated as:

$$x'(t) \approx \frac{x(t + \Delta t) - x(t)}{\Delta t} \quad (2.28)$$

$$x''(t) \approx \frac{x'(t + \Delta t) - x'(t)}{\Delta t} = \frac{x(t) - 2x(t + \Delta t) + x(t + 2\Delta t)}{\Delta t^2} \quad (2.29)$$

By reversing the time step (i.e. use  $-\Delta t$ ) to approximate the velocity and acceleration based on the previous time steps we can discretize the position by taking finitely small time steps (i.e.  $x(t) = x_i$ ,  $x(t - \Delta t) = x_{i-1}$ ). The same cannot be done for white noise as no information is known about  $W(t)$  at any time. We can instead say that the velocity of a Brownian particle should approximate our white noise as a random walk, where at each new time step the position changes randomly within a given range. Constricting the variance to  $\sqrt{2D}/\Delta t$  allows us to represent the white noise using the finite-difference approach as:

$$m \frac{x_i - 2x_{i-1} + x_{i-2}}{\Delta t^2} = -\gamma \frac{x_i - x_{i-1}}{\Delta t} + \sqrt{2k_B T \gamma} \frac{w_i}{\sqrt{\Delta t}} \quad (2.30)$$

Where  $w_i$  is a random real number between -1 and 1, we can say that it is normally distributed around 0 for simulation purposes. We can rearrange this for  $x_i$  to approximate the Brownian motion of a particle (setting  $x_0 = 0$ ), where the characteristic time is  $\tau = m/\gamma$ . Now in the case of an optical trap the restoration time scale is given by  $\tau_{OT} = \kappa_x/\gamma$  which for strongly trapped particles is far greater than the characteristic time, therefore for simulation purposes we can neglect the particle's inertia which allows

## Chapter 2. Theory and methods

us to write the motion of an optically trapped particle as:

$$x_i = x_{i-1} + \tau_{OT} x_{i-1} \Delta t + \sqrt{2D\Delta t} w_i \quad (2.31)$$

This result can be generalised for a 3-dimensional description of an optically trapped particle, where each Cartesian direction has its own unique characteristic restoration time. We see from the result that trajectory is dependent on only a handful of factors, the trap stiffness  $\kappa_x$ , the fluid viscosity  $\gamma$ , and the thermal energy of the system  $k_B T$  - with the latter two being related by Einstein's formulation of the diffusion coefficient  $D = k_B T / \gamma$ . Therefore by calculating these parameters to a high degree of precision allows one to get precise description of the forces experienced by a target particle, which in the past has been used for highly accurate force transduction [47, 48].

## 2.5 Calibration Techniques

There are several approaches for calibrating and characterizing the optical trap, each approach has its drawbacks and benefits so each option should be chosen based on what elements want to be characterized. The basis for each of these methods stems from the analytical solution of the Langevin equation:

$$x(t) = x(0)e^{-t/\tau_{OT}} + \sqrt{2D} \int_0^t ds W_x(s) e^{-(t-s)/\tau_{OT}} \quad (2.32)$$

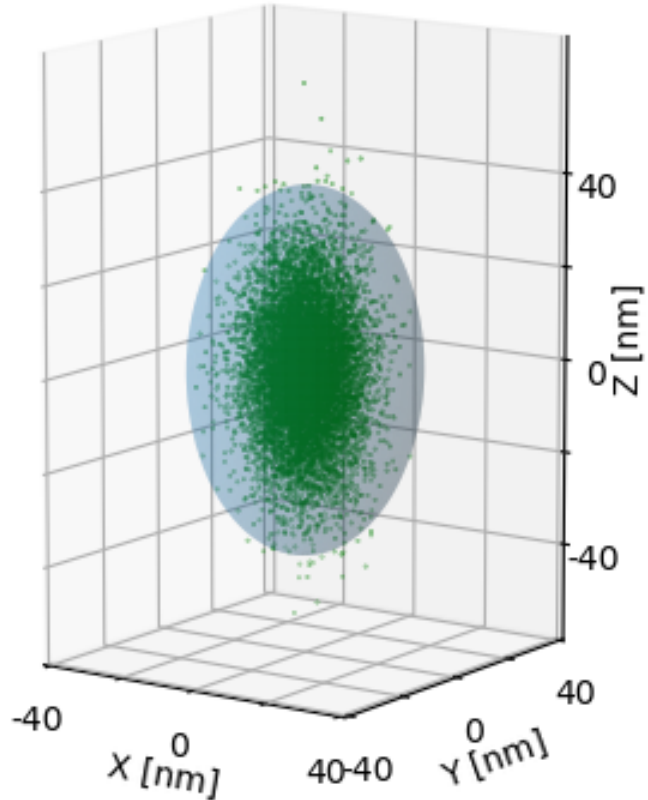


Figure 2.2: Example trajectory created using Finite Differences method for a  $2\mu\text{m}$  diameter sphere. Trap stiffness's were estimated using *ott* at  $\kappa_x = \kappa_y = -100 \text{ pN}/\mu\text{m}$  and  $\kappa_z = -25 \text{ pN}/\mu\text{m}$ . The particle's motion can be localised around the shaded ellipsoid.

### 2.5.1 Potential Well Analysis

The Langevin equation for an optically trapped assumes that the trap acts similar to a Hookean spring that creates a potential well about its centre. Therefore a simple analysis method is to understand the height and width of said potential well.

Potential analysis is a useful technique for estimating the strength of an optical trap; this method assumes that the force acting on the particle is purely conservative, an accurate presupposition if we ignore the motion of the particle as it enters the trap.

## Chapter 2. Theory and methods

This is because the scattering force is far more significant far away from the potential well and is negligible if the trap strength is much greater than the thermal fluctuations.

With this in mind we can write the probability of finding the particle at position  $x$  as:

$$\frac{\rho(x)}{\rho_0} = e^{-\frac{U(x)}{k_B T}} \quad (2.33)$$

which therefore means we can write the potential well as:

$$U(x) = -k_B T \ln \left( \frac{\rho(x)}{\rho_0} \right) \quad (2.34)$$

Now assuming our laser acts as a Gaussian beam we should be able to describe the probability distribution  $\rho(x)$  centred at some equilibrium position  $x_0$ :

$$\rho(x) = \sqrt{\frac{\kappa_x}{2\pi k_B T}} \exp \left( -\frac{\kappa_x}{2k_B T} (x - x_{eq})^2 \right) \quad (2.35)$$

By inserting eq. 2.35 into eq. 2.34 we can fit the potential well in order to determine the trap strength  $\kappa_x$ , and an estimation of the equilibrium position  $x_{eq}$ . This has some limitations in that the large fluctuations can throw off the fit meaning a longer acquisition time is necessary to properly fit the potential well, making it difficult to characterise weakly trapped particles who may not remain trapped for long. It also provides no information on the particle itself (i.e. the friction coefficient  $\gamma$  and diffusion coefficient  $D$ ).

### 2.5.2 Equipartition method

The Equipartition method is by far the fastest and simplest means for estimating the trap strength but unlike Potential Analysis is limited strictly to harmonic potentials. This can be often not the case for highly focused beams, as the trap strength can vary due to polarisation differences. Simply put we can use the equipartition theorem to relate the potential well to the particle's thermal energy using eq. 2.35:

$$\langle U(x) \rangle = \frac{1}{2} \kappa_x \langle (x - x_{eq})^2 \rangle = \int_{-\infty}^{\infty} \rho(x) (x - x_{eq})^2 = \frac{1}{2} k_B T \quad (2.36)$$

$$\implies \kappa_x = \frac{k_B T}{\langle (x - x_{eq})^2 \rangle} \quad (2.37)$$

By taking a time average over multiple trajectories to get  $\langle x - x_{eq} \rangle$  we can get a fairly accurate estimation of the trap strength. Because of this requires a time average of the particle's displacement any large errors in the position measurement can have knock-on effects. Likewise with the potential analysis route, no information is gleaned about the particle itself.

### 2.5.3 Mean Square Displacement

Mean square displacement (MSD) is a common means of describing the random motion of a given particle (or group of particles). This is useful information if say for example we want to understand reaction kinetics on the surface of a catalyst, if we know how far its likely to move from the surface we can tell if its likely to react when a catalytic site becomes available. As it pertains to colloids, consider a suspension of silica spheres immersed in a fluid undergoing Brownian motion (as described by the

## Chapter 2. Theory and methods

Langevin Equation) so that:

$$mx''(t) + \gamma x'(t) = \eta(t) \quad (2.38)$$

Where  $\gamma$  is the objects friction coefficient which for spheres is given as  $\gamma = 6\pi\eta r$ , and  $\eta(t)$  is a random white noise variable that is directly related to the thermal energy of the surrounding fluid. If the motion is truly random then we should see an average displacement of 0 regardless of how long we measure for. If we wish to understand the effects of a given external factor (i.e. an electric field or localised heating), simply looking at displacement will reveal nothing of value as its difficult to differentiate between diffusive and a biased motion.

For each sphere we can record its position in the  $x - y$  plane and measure its displacement from a set reference point; for example with an optical tweezer this could be the beam focus. We can measure the MSD by forming a 'window' between two points in time of the trajectory (i.e.  $t & t + \tau$ ) and sliding this window along the entire trajectory length - to eliminate -ve displacements we take the square - we can then take the average of this series. Repeating over a range of time lags allows us to describe the MSD as a function of  $\tau$ :

$$MSD(\tau) = \langle |x(t + \tau) - x(t)|^2 \rangle \quad (2.39)$$

If we use eq. 2.32 for an optical tweezer we can expand out the squared term to get

## Chapter 2. Theory and methods

an analytical expression for the MSD as a function of time lags:

$$MSD(\tau) = \langle |x(t + \tau)^2 - 2x(t + \tau)x(t) + x(t)^2| \rangle = \frac{2k_B T}{\kappa_x} \left[ 1 - e^{-\frac{\tau}{\tau_{OT}}} \right] \quad (2.40)$$

From this expression it's evident that the mean squared displacement increases with larger values of  $\tau$  until it reaches a maximum value as shown below by the dotted line.

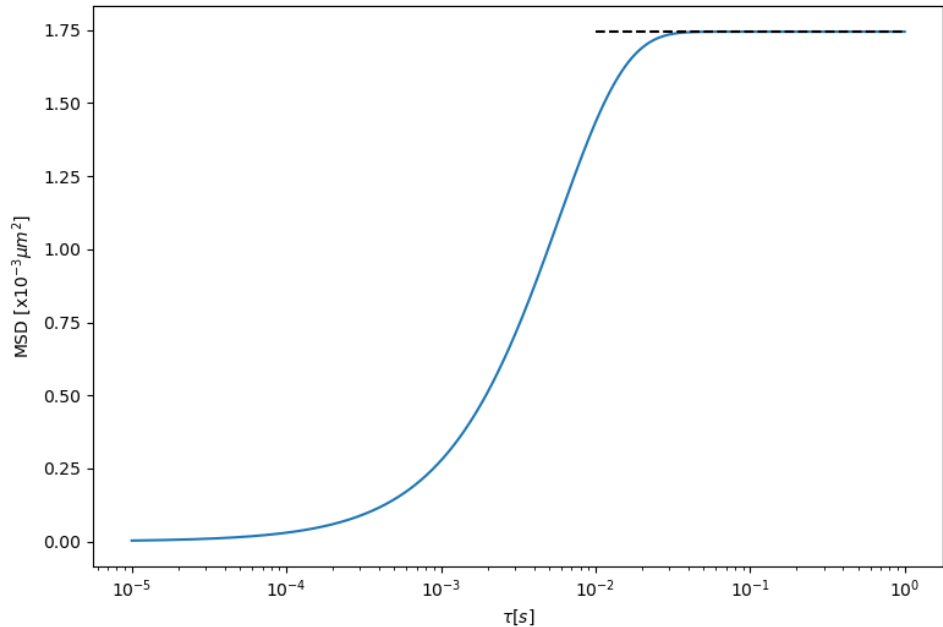


Figure 2.3: Example mean squared displacement using eq. 2.40, for a  $1\mu m$  sphere trapped by an optical potential well. The dotted line represents the upper limit of the sphere's displacement due to the optical trap.

The MSD plot can be subdivided into two regimes, when  $\tau \gg \tau_{OT}$  the particle is experiencing the harmonic potential described by the equipartition theorem, and when  $\tau \ll \tau_{OT}$  the particle is said to be freely diffusing within the trap focus. Of course for

## Chapter 2. Theory and methods

a freely diffusing object the MSD will never reach a plateau value, comparing MSD's for different particles provides a simple visual indicator of the difference in trapping strength. The MSD method is an already very versatile analytical tool for diffusive motion, however it is rather slow in computing time meaning it is only really beneficial when a high degree of accuracy is required and shorter time resolutions are unavailable - such as using a quadrant photo diode instead or a high speed CCD.

### 2.5.3.1 Angular Mean Square Displacement (MSAD)

It is also possible to plot the angular MSD (MSAD) using simulative data, however there is yet to be a analytical expression for the MSAD of a freely diffusing particle. Vigilante *et al* [49] derived the upper limit of a dimer's MSAD along its long axis by assuming it was strongly trapped and so had limited angular motion, there expression gives:

$$\lim_{\tau \rightarrow \infty} \langle (\Delta u_z)^2 \rangle = 2 \left[ 1 - \frac{1}{4\beta\kappa_r} \left( \frac{\exp(\beta\kappa_r) - 1}{\exp(\beta\kappa_r)F(\sqrt{\beta\kappa_r})} \right)^2 \right] \quad (2.41)$$

Vigilante's paper expressed that they couldn't compute  $MSD(\tau)$  because they couldn't solve the Einstein-Smoluchowski equation which describes the diffusion constant for dielectric particles. This would require a full description of a particle's electrical mobility and charge distribution - the latter could be achieved via a discrete dipole approximation, the former would be dependent on both the particle's position but relative orientation to the electric field.

### 2.5.4 Power Spectrum Density (PSD)

The power spectral density (PSD) method is by far the most versatile method for observing the dynamics of any object within an optical trap, allowing for fast calibration times while also quickly filtering out typical noise sources. Taking the Fourier transform of a particle's trajectory yields:

$$\hat{x}(f) = \frac{(2D)^{1/2}\hat{\eta}}{2\pi(f_c - if)} \quad (2.42)$$

where  $\hat{\eta}$  is the Fourier transform of the white noise, where the values are exponentially distributed as opposed to being normally distributed in the time domain [47], the correlation function is given as:

$$\langle \hat{\eta}_k \hat{\eta}_l^* \rangle = t_{msr} \delta_{k,l} \rightarrow \langle \eta^4 \rangle = 2t_{msr} \quad (2.43)$$

We can therefore ignore the white noise from our analysis by looking at the spectral density of  $\hat{x}(f)$ :

$$S_x = \frac{\hat{x}^2}{t_{msr}} = \frac{D}{2\pi(f_c^2 + f^2)} \quad (2.44)$$

We can fit the Lorentzian via a simplified geometric series  $S_x = 1/(A + Bf_k^2)$  which allows us to compute both the diffusion coefficient (in arbitrary units) and the corner frequency  $f_c$  which is directly related to the trap strength via  $f_c = \kappa_x/(2\pi\gamma)$ . Like with the analytical expression of the mean squared displacement we see two distinct regions, when  $f \ll f_c$  the PSD reaches a plateau value that when converted to length

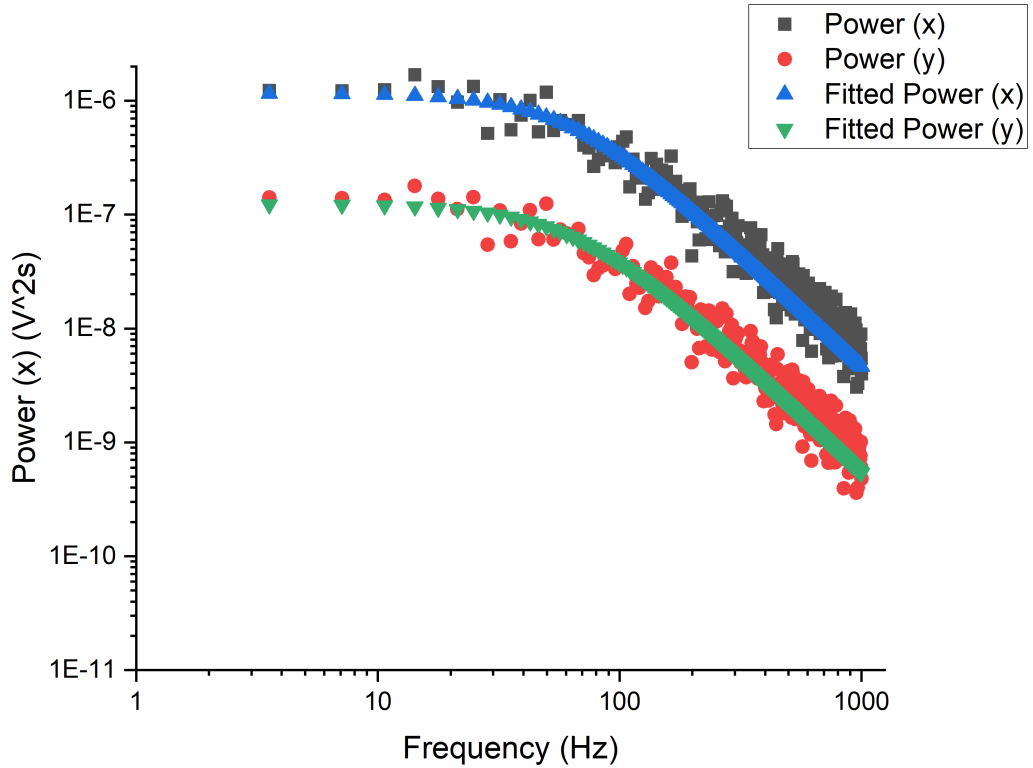


Figure 2.4: Example PSD fitted using Eq. 2.44, power spectra is collected from an optically trapped silica sphere suspended in water. The difference in magnitude is due to the asymmetry of the quadrant photo diode having a stronger signal response in the direction of the polarisation vector. Using a correction factor (see Eq. 2.46) will adjust the power spectra to better describe the trap shape.

units represents the maximum displacement the particle can move beyond the focus, however when  $f \gg f_c$  the PSD falls off exponentially which denotes the particle is freely diffusing within the beam focus.

The Lorentzian relationship is only valid for frequency terms up to the Nyquist frequency (half of our sampling rate), this is because we are only taking a finite sampling of the particle's trajectory meaning the signal is aliased. Berg and Sorensen provide a

## Chapter 2. Theory and methods

suitable modified Lorentzian to account for the aliasing effects [47]:

$$S_x = \frac{(\Delta x)^2 \Delta t}{1 + c^2 - 2c \cos 2\pi f_k \Delta t / N} \quad (2.45)$$

Where  $N$  is the total number of samples taken,  $\Delta x$  &  $c$  have no direct physical interpretation and are defined in [47]. Further modifications can be made to the power spectrum model but this is only useful when a high degree of accuracy is necessary. Typically power spectra are recorded using a Quadrant Photo Diode (QPD), which records motion in voltage units, not in units of length. To convert between the two we have a few methods: Firstly if we have a mono-disperse suspension of particles, the laser can be scanned across the surface of our target particle; so long as the particle's size is known a linear conversion factor can be used to convert from voltage to length units. Secondly, if the size distribution is very wide but each particle can be accurately sized, then a conversion factor can be approximated by comparing the fitted value of the diffusion coefficient, and the reported value given by the Stokes-Einstein relation.

$$D_{SE} = \frac{k_B T}{\gamma_0} \Rightarrow \text{Conversion Factor } [m/V] = \sqrt{\frac{D_{SE}}{D_{fit}}} \quad (2.46)$$

With the latter method, the local fluid viscosity must be known to a high degree of accuracy, depending on the local heating effect this may be as trivial increase or it may be significant enough to drastically alter the characterisation. PSD analysis is often seen as the gold standard for calibration as it can be fine tuned to the point that optical forces can be computed on the order of  $10^{-15} N$  [47], it captures all of

the information acquired by other calibration techniques while filtering out noise and requiring a relatively small amount of data collected.

## 2.6 Simulation of spherical aggregates

Later chapters cover the dynamics of spherical aggregates and anisotropic scatterers, these subjects are particularly difficult to characterise using conventional calibration techniques [50, 51]. As an example consider a symmetric dimer as a paradigmatic aggregate; if we consider the Langevin equation for such a aggregate within an optical trap we have:

$$\frac{d\vec{r}(t)}{dt} = \frac{\vec{\kappa}_x}{\gamma} \vec{r}(t) + \sqrt{2\vec{D}_x} \eta(t) \quad (2.47)$$

Where  $x(t)$  is replaced with  $\vec{r}(t)$  to signify that the translational motion is generalised to a 3 dimensional case. Except now, the dimer is undergoing random rotational motion in addition to its Brownian translational motion the first term on the right hand side is no longer purely a function of the dimer's position but also on its orientation. The rotational form of the Langevin equation for a dipole within an external potential is given as:

$$\frac{d\vec{u}(t)}{dt} = \frac{\mu}{\gamma_R} [\vec{u}(t) \times \vec{E}(t)] \times \vec{u}(t) + \sqrt{2\vec{D}_R} \lambda(t) \times \vec{u}(t) \quad (2.48)$$

Where  $\vec{u}(t)$  is the unit vector aligned along the centres of the two spheres,  $\mu$  is its dipole moment, and  $\gamma_R$  is the rotational friction coefficient which is given as  $\gamma_R = 8\pi\eta r^3$

## Chapter 2. Theory and methods

for a sphere, if the dimer is within a harmonic potential we can write the first term on the right hand side as  $\frac{\vec{\kappa}_u}{\gamma} \times \vec{u}(t)$ , where  $\vec{\kappa}_u$  is the rotational stiffness vector.  $\lambda(t)$  is the Brownian rotations from the surrounding fluid, like in the translational case the Brownian rotations are normally distributed and are also uncorrelated so that:

$$\langle \lambda(t)\lambda(t') \rangle = \delta_{ij}\delta(t-t') \quad (2.49)$$

For an asymmetric scatterer whose radius is comparable to that of the electric field's wavelength we now have a system of simultaneous equations:

$$\frac{d\vec{r}(t)}{dt} = \frac{\vec{\kappa}_x(\vec{u}(t))}{\gamma} \vec{r}(t) + \sqrt{2D}\eta(t) \quad (2.50)$$

$$\frac{d\vec{u}(t)}{dt} = \frac{\vec{\kappa}_u(\vec{r}(t))}{\gamma_R} \times \vec{u}(t) + \sqrt{2D_R}\lambda(t) \times \vec{u}(t) \quad (2.51)$$

Fortunately, we do not need to solve these directly as the latter two random variables can be easily approximated if the thermal energy of the system is known, and the rate of change can be assumed as linear if we take a sufficiently small time step that  $\Delta t \ll \kappa_x/\gamma$  &  $\Delta t \ll \kappa_u/\gamma_R$ . In doing so we now only need to compute the optical force and torque applied to our dimer, this has already been compiled in a MATLAB package called *Optical Tweezer Toolbox* or *ott* [52]. In which they use the results from [53] to compute both the optical force and torque using the beam coefficients - the form given

## Chapter 2. Theory and methods

by [54] is an easier form to compute:

$$\begin{aligned} \mathbf{F}_z = & -\frac{1}{4\pi k^2} \sum_{n,m} \left( \frac{m}{n(n+1)} \Im[a_{nm} b_{nm}^* - p_{nm} q_{nm}^*] \right. \\ & + \frac{1}{n+1} \left[ \frac{n(n+2)(n-m+1)(n+m+1)}{(2n+1)(2n+3)} \right]^{1/2} \\ & \times \Im[b_{nm} b_{nm}^* + a_{nm} a_{n+1m}^* - q_{nm} q_{nm}^* + p_{nm} p_{n+1m}^*] \end{aligned} \quad (2.52)$$

$$\begin{aligned} \mathbf{T}_z = & -\frac{1}{8\pi k^3} \sum_{n,m} \left( \frac{m}{n(n+1)} [|a_{nm}|^2 + |b_{nm}|^2 - |p_{nm}|^2 - |q_{nm}|^2] \right. \\ & + \frac{2}{n+1} \left[ \frac{n(n+2)(n-m+1)(n+m+1)}{(2n+1)(2n+3)} \right]^{1/2} \\ & \times \Re[b_{nm} a_{nm}^* + a_{nm} b_{n+1m}^* - p_{nm} q_{nm}^* + q_{nm} p_{n+1m}^*] \end{aligned} \quad (2.53)$$

where  $a_{nm}$ ,  $b_{nm}$ ,  $p_{nm}$ , and  $q_{nm}$  are the beam coefficients of the incident and scattered fields respectively. We can get the transverse force and torque components in a similar form by applying a simple rotation transformation. In order to get the scattered beam coefficients we can use *mstm* [38] to calculate the T-matrix of our dimer (or any spherical aggregate). Vigilante et al compiled together a python package that combines both *ott* and *MSTM* to simulate the behaviour of spherical aggregates within a predefined optical trap.

Throughout this PhD we use the work of Vigilante to perform a systematic study of the dynamics demonstrated by asymmetric dimers in both plane and circularly polarised light. But furthermore we expand upon their work to create a fully functional quadrant photo-diode to simulate the response from a calibration test. This builds upon the work from [2] which applied the fundamental principles of Lorenz-Mie theory to replicate the response signal of a QPD being used in back focal-plane interferometry.

### 2.6.1 Simulated Quadrant Photodiode

In order to simulate a typical experimental set up with a QPD installed as a position detection system we need to evaluate the total magnitude of the electric field incident on the photo-diode surface. While trapping a micro-particle, the scattered and incident fields combine together and interfere with one another. These fields are collected by a condenser lens in the far field limit and are focused onto the QPD surface, the total intensity can be evaluated as:

$$I(x, y) = \epsilon_0 c \left| \begin{bmatrix} E_{i,x}(x, y) + E_{s,x}(x, y) \\ E_{i,y}(x, y) + E_{s,y}(x, y) \\ E_{i,z}(x, y) + E_{s,z}(x, y) \end{bmatrix} \right|^2 \times \text{step}(NA_c - \sqrt{x^2 + y^2}) \quad (2.54)$$

The last term is simply a representative step term that defines the outer limit by which we evaluate the electric field, this is analogous to our condenser lens removing noise from other light sources by only accepting light at a specific acceptance angle defined by its numerical aperture  $NA_c$ . Depending on the relative size of our particle we can adjust the acceptance angle, this has very little effect on the transverse signals, but for axial evaluations of a trapped particle the numerical aperture should be tuned so that the resultant response curve has negative slope in order to allow for axial position detection, the method for finding this angle  $\theta_\Theta$  is discussed in [55].

The incident beam is simple enough to define given our set up parameters, for the sake of simplicity we assume that our beam is a Laguerre-Gaussian beam of mode  $[0.0, 0.0]$  (which is simply a pure Gaussian beam). *Ott* uses a point matching approach

## Chapter 2. Theory and methods

to approximate the beam shape coefficients of the incident field by fitting it to the far field estimate, the beam is of the form:

$$E_{\text{inc}}(kr) = \sum_n^{\infty} \sum_{m=-n}^n a_{mn} Rg M_{nm}(kr) + b_{nm} Rg N_{nm}(kr) \quad (2.55)$$

where  $RgM_{nm}(kr)$  &  $RgN_{nm}(kr)$  are regular vector spherical wave functions, these differ from Eq. 2.11 in the fact that the field can either be expressed as an incoming/outgoing wave (with a singularity at the origin) or as a regular wave around the origin; for incoming/outgoing waves the wave functions use the first/second forms of the Hankel function respectfully. In order to compute the regular spherical wave at the origin we replace the Hankel function with the Bessel function which is simply the average of the first and second forms of the Hankel function, so at the origin we avoid a singularity of the EM field.

We can if we want further restrict the incident beam by applying setting the truncation angle to match our microscope object, this essentially applies a cut off point to the In order to compute the scattering from the target particle *ott* uses the *T*-matrix method, this is not essential for a simple sphere but is essential for complex shaped particles such as dimers. The matrix from *mstm* needs to be repackaged to work with the *ott* software, converting it from a column vector into a system of sub matrices.

The scattered and incident fields are then combined together in the far field to get

## Chapter 2. Theory and methods

$I(x, y)$ , the quadrant and overall signals are calculated via:

$$Q_i = \sum_{n,m} I(x_{i,n}, y_{i,m}) \quad (2.56)$$

$$S_x = \frac{(Q_1 + Q_2) - (Q_3 + Q_4)}{\sum I_0(x, y)} \quad (2.57)$$

$$S_y = \frac{(Q_1 + Q_3) - (Q_2 + Q_4)}{\sum I_0(x, y)} \quad (2.58)$$

$$S_z = \frac{(Q_1 + Q_2 + Q_3 + Q_4)}{\sum I_0(x, y)} \quad (2.59)$$

Where the denominator is the total intensity on the QPD while there is no particle within the trap. The QPD sensitivity is dependent on both the polarisation of the incident beam and the displacement of the target sphere, this is shown in fig. 2.5.

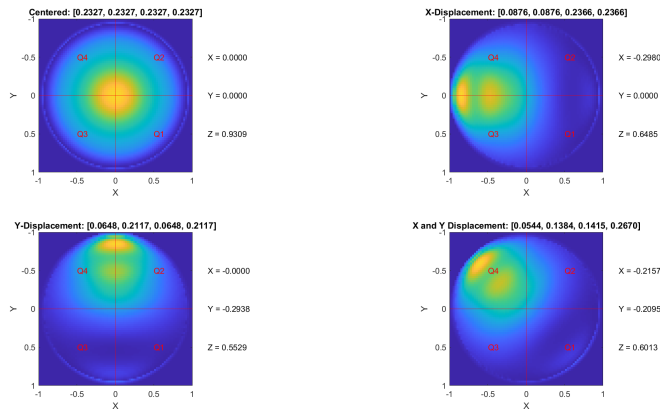


Figure 2.5: Total Field incident on the quadrant photo diode for several different displacements. Top Left:  $2\mu m$  diameter silica sphere placed at the focus of a beam. Top Right: silica sphere is now displaced by  $1\mu m$  along the x-axis. Bottom Right: silica sphere is now displaced by  $1\mu m$  along the y-axis. Bottom Left: silica sphere is now displaced by  $0.707\mu m$  along the x and y axis. The trapping beam is a  $TEM_{00}$  Gaussian, polarised along the along the x-axis.  $S_x$ ,  $S_y$ , and  $S_z$  are shown to the right of each graph,  $Q_1$ ,  $Q_2$ ,  $Q_3$ , and  $Q_4$  are shown above each graph.

Rather than displacing and rotating the particle itself, we instead rotate and dis-

## Chapter 2. Theory and methods

place the incident beam and recalculate the beam coefficients; the total beam is then inversely rotated in order to record the QPD signal. This ensures that for a homogeneous sphere, even if the sphere itself undergoes rotation the QPD signal is unaffected by the change in orientation.

To confirm that our method is producing accurate results, we ran a comparison between our simulative QPD and the results from [2]. Where a  $300\text{ nm}$  diameter sphere is scanned across the path of a focused Gaussian beam ( $\lambda = 1064\text{ nm}$ ,  $NA = 1.2$ ), the sphere has a refractive index of 1.57 and is suspended in water ( $n_{med} = 1.33$ ) and the condenser lens has its numerical aperture set to 0.5 ( $\theta_{max} = 30^\circ$ ). Scanning across all three primary axis produced the following response curve.

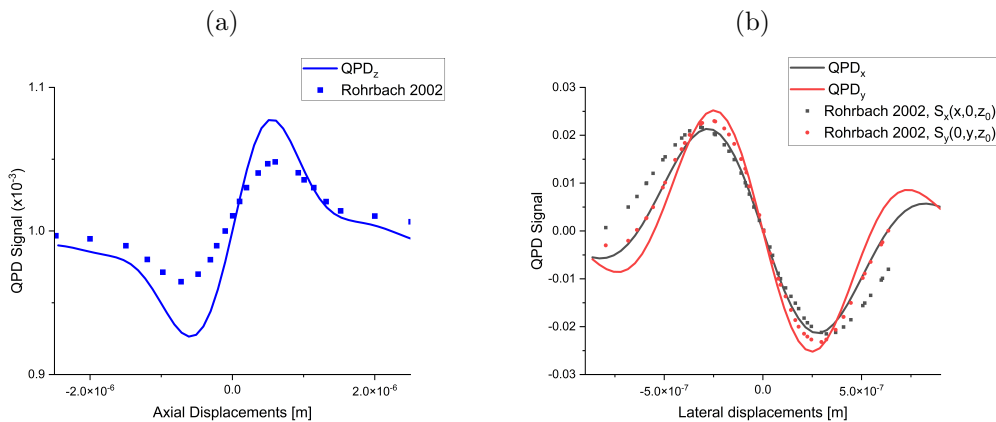


Figure 2.6: Comparison between QPD response signal versus work conducted by Rohrbach, single sphere ( $r = 150\text{ nm}$ ,  $n = 1.57$ ) is scanned by a  $1064\text{ nm}$  laser and the QPD signal recorded. Solid lines represent the signal produced by QPD using *ott* and points represent the signal response collected from [2].

With this any trajectory can be collected from the QPD by displacing and rotating the beam accordingly, later in chapters 4 and 5 we discuss how to extract information from the QPD's signal.

## **Chapter 3**

# **Effects of localised shearing on crystal growth and nucleation**

As outlined in Chapter 1, the original outline of the PhD was to investigate the possibility of using optical tweezing as a means of initiating and controlling nucleation by generating fluid flow within a small droplet of supersaturated solution. The goal of which would be to understand the influence of shearing on nucleation at a micro level as compared to larger scale results. It has been shown that for macro-scale systems, the likelihood of nucleation increases to a maximum value under increased shearing [12,13]. Theoretical research into the matter identified two competing effects that effect a crystal in moving fluid fields; firstly, nucleation is enhanced due to the increased mass transfer of solute material; and secondly, shear flow against the crystal surface leading to a decrease in growth [13]. These two competing effects are validated by experimental work using glycine solutions, showing that beyond a certain shear rate the nucleation rate is reduced [12]. In this chapter I outline the optical tweezer equipment used during

this PhD, the initial attempts made to induce nucleation via optical rotation, and the impact of a moving beam on the crystal growth of a newly formed nucleus.

### 3.1 Optical Tweezer Equipment

In general, all optical tweezers require a laser driver, two microscope objectives (one for trapping and one for imaging), and a means of controlling the position of the loaded sample. While there are other pieces of equipment used in modern tweezer experiments these are the bare minimum requirements for any optical tweezer. The laser used for this project was a 1064 nm near infrared laser - provided by CNI Lasers – that has an adjustable power supply to vary the energy output of the laser - the remaining optics where supplied by Thor Labs. Experimental work has shown that the trapping efficiency increases with beam diameter up until it exceeds  $\frac{2}{3}D_{obj}$  [56] where  $D_{obj}$  is the diameter of the objective aperture. To expand the beam front we utilise a Galilean beam expansion arrangement (indicated by  $f_1$ , and  $f_2$ ) as recommended for high power laser applications. In our initial experiments the beam expansion provides a  $4\times$  magnification; however, in later experiments where we utilise a galvano-mirror the beam expansion is  $3\times$  and then the 4f correlator provides a further  $1.25\times$  magnification (using  $f_3$  and  $f_4$ ) - where the magnification is given by.

$$\frac{D_2}{D_1} = \frac{f_2}{f_1} \quad (3.1)$$

It should be noted that the galvano-mirror requires the use of a Keplerian beam expansion arrangement which reduces the transmitted laser power due to localised heating

of the air. Afterwards the laser is passed through a dichroic mirror that separates incoming infrared and visible light, this is to prevent the laser from damaging the CCD camera used for imaging the trapping plane. The laser is then focused to a diffraction limited spot by a 1.25 NA objective. By increasing the numerical aperture of the objective, the gradient force at the focal point is increased; the trade-off being that the for higher NA values the trapping depth is reduced due to spherical aberrations. While it is possible to increase the trapping depth [57] by adjusting the objective's tube length this approach is incompatible with our trapping arrangement. A 0.25 NA condenser objective refocuses the scattered laser light and also provide an aperture for an imaging LED to illuminate the focal plane. Samples are loaded onto a piezo driven table to that is inserted between the trapping and condensing objectives; the piezo drivers allow for sub-micron control of the sample position to a degree as small as a 10 nm. To detect and monitor the position of a trapped particle a quadrant photo diode (QPD) was utilised.

### 3.1.1 Position detection methods

In order to accurately capture the dynamics of a trapped particle, a position detection system must be utilised. There are 3 possible methods of position detection: video-analysis, lateral-effect position sensing, and quadrant photodiodes. The former being ideally suited for multiple traps or situations where precision is not the top priority. In order to match the force measurements of back-focal plane interferometry requires the camera's frame rate to exceed 1  $kH\bar{z}$  which can be difficult to achieve while maintaining a decent resolution [58]. In comparison off the shelf back-focal plane detectors can

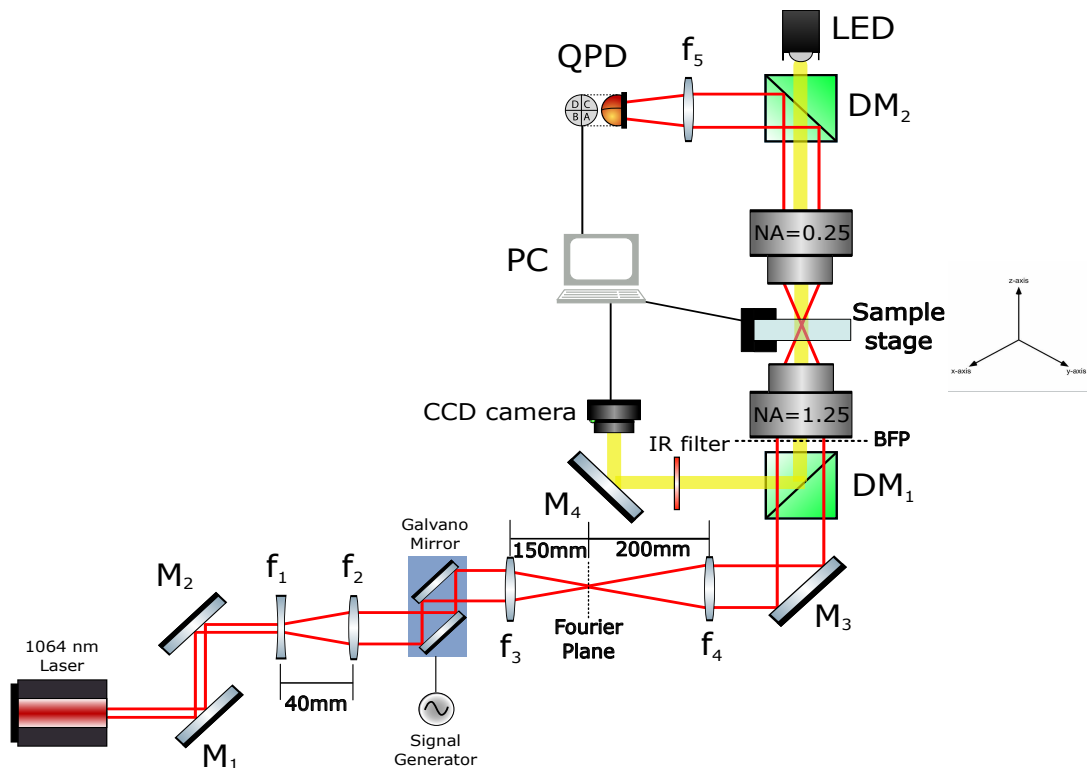


Figure 3.1: Optical tweezer set up used for the majority of the PhD. The focal lengths of  $f_1$ ,  $f_2$ ,  $f_3$ , &  $f_4$  are  $-20\text{ mm}$ ,  $60\text{ mm}$ ,  $150\text{ mm}$ , &  $200\text{ mm}$  respectively. Diagram not drawn to scale.

achieve temporal resolutions anywhere from  $10 - 100 \text{ kHz}$ .

A QPD is frequently used position detection system for optical tweezers due to their high sampling rate, high degree of precision, and ease of set up. The QPD is constructed of four photo diodes assembled in a quadrant formation, when a particle is trapped the interference pattern produced is focused onto the QPD, with the maximum intensity mapping to the particle's centre of mass. By summing the voltages of the horizontal and vertical quadrants together the particle's centre of mass is tracked in the x-y plane. Axial displacement can be estimated by observing the change in the total voltage of the QPD. The outputted signal gives an indication of the particle's relative displacement from the beam focus, but in order to convert the signal to distance units the trap needs to be calibrated (assuming a linear response curve).

A lateral-effect sensor has a similar output but works using a the entire sensor as a single cell analogous to the focal plane of the trapping beam. The four corners of the sensor act as anodes connected to a base plate cathode, as the beam moves across the surface of the detector each anode will experience a different photocurrent depending on how close the centre of the interference pattern is to each anode. The advantage of a lateral effect detector is that the linear regime is much larger than a QPD making it much better for monitoring the position of a trapped particle. However, Lateral-effect sensors are often limited in their spacial resolution due to high signal-to-noise ratios, requiring a high intensity of light on the sensor in order to get a clean signal. As a result, most optical trapping experiments are conducted using a QPD as opposed to a lateral-effect sensor, as often the displacement is small enough that the QPD response curve can be considered linear.

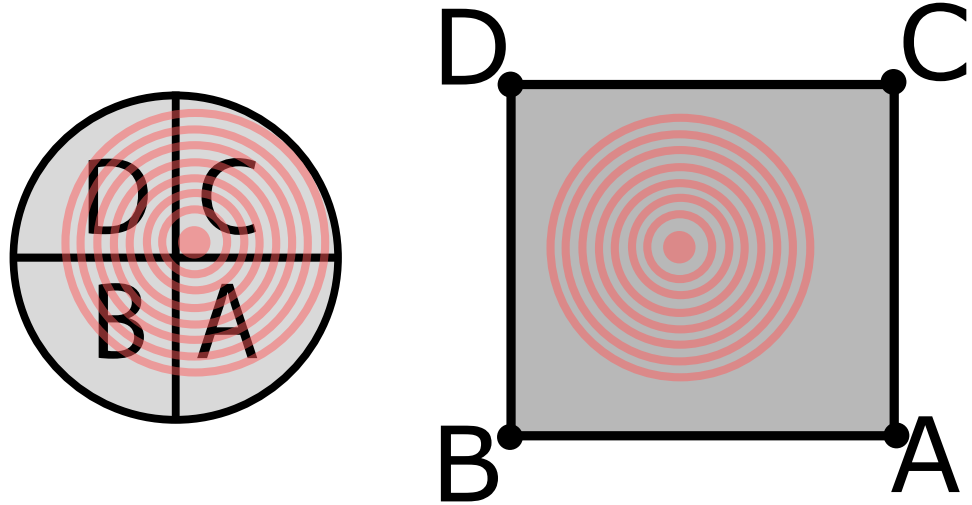


Figure 3.2: Comparison between QPD and Lateral effect photodiodes. The four quadrants of a QPD (left) experience different photocurrents based on the total intensity of light incident on each section (labelled A, B, C, D). Whereas a Lateral effect sensor (right) uses the resistive properties of the photodiode surface to vary the create different photocurrents passing through the anodes A, B, C, and D.

### 3.1.2 Fourier Optics and 4f correlators

A 4f correlator is an example of Fourier optics in practice, understanding that a focused lens takes a Fourier transform of the light profile. Consider a laser with a circular Gaussian profile, if you were to place a detector there you would pick up the intensity as a function of its position within the beam. If however you focused the light into a single point (using a +ve focal lens) you are actually seeing a measurement of the phase of your laser with position, in which you would see a diffraction limited spot ( $d = \lambda/2n\sin(\theta)$ ), indicating that the laser is collimated. In imaging systems, a series

of focal lenses can be used to filter out unwanted scattering from an image (or in an inverse case differentiate between different images), the placement of each lens is shown below. For our applications a 4f correlator is utilised to ensure that the motion of the galvano-mirrors does not move the focal point of the laser, allowing for a stable trap even while in motion.

## 3.2 Calibration of Tweezer Setup

Prior to testing optical rotation the trapping laser was calibrated using power spectra analysis

## 3.3 Synthesis of Birefringent Micro spheres

Generation of fluid shear can be achieved via two avenues: Firstly, by utilising circularly polarised light it is possible to transfer angular momentum from the laser to the trapped entity. Secondly, one can directly move the trap within the imaging plane by steering the beam using either a galvanometric mirror or gimbal mirror. The following chapter outlines the work done with shear generated by circularly polarised light and the challenges of applying this to localising nucleation.

There are several options for particles that can be rotated using optical tweezers [59, 60]. Over the course of the PhD two different micro spheres where investigated, vaterite and liquid crystal droplets. Both can be readily synthesised in the lab and are will rotate at a variety of sizes. While silver nano particles were considered their high cost and small size meant they were disregarded as an option for optical rotation.

### Chapter 3. Effects of localised shearing on crystal growth and nucleation

Vaterite is a polymorph of calcium carbonate that is rarely seen in nature due to its low stability. However unlike its other polymorphs of calcite and aragonite, when synthesised vaterite will typically form small spherical particles making them ideal for optical trapping and rotation. Synthesis of vaterite micro spheres requires fine control of the nucleation process in order to maintain polymorphic stability, though for the purposes of optical rotation the exact polymorph is not as important as its morphology as all 3 polymorphs are inherently birefringent.

Vaterite samples were made by the first preparing equal amounts of  $CaCl_2$  and  $Na_2CO_3$  at a concentration of  $0.33M$ , at the same time a vial of  $0.33M\ MgSO_4$  was prepared and set aside for later. First a small vial was filled with  $1.5mL$  of  $CaCl_2$  followed by  $60\mu L$  and  $90\mu L$  of  $MgSO_4$  and  $NaCO_3$  respectively, forming a seed solution. Next, a larger vial was filled with  $5\ mL$ ,  $1.5\ mL$ , and  $1\ mL$  of  $CaCl_2$ ,  $MgSO_4$ , and  $NaCO_3$  respectively followed by the seed solution. After 10 minutes of slow but continuous mixing a few drops of Agepon was added to halt the reaction, the solution was filtered and washed 3 times with distilled water before being suspended in water. When trapped in circularly polarised light, the anisotropic scattering of the sphere results in a periodic signal on the QPD. Therefore, the resulting power spectrum is not a Lorentzian but now also displays peaks that appear at integer multiples of the particles rotational frequency.

Liquid crystals are an intriguing example of materials with mixed phase properties, unlike typical solutes such as Glycine, a liquid crystal can still maintain some degree of order between its individual molecules while in the liquid state. This is due to the fact that liquid crystals are constructed of long ordered molecules that demonstrate

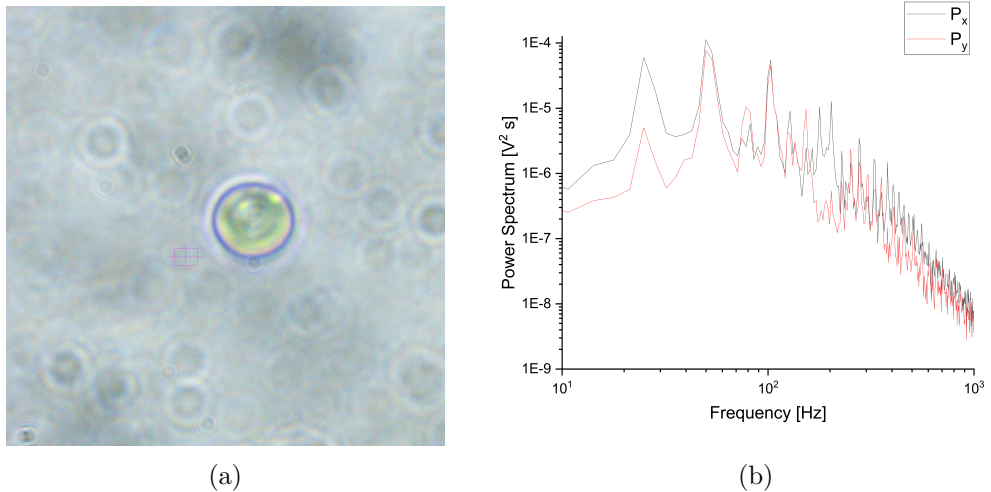


Figure 3.3: (a) Sample vaterite sphere suspended in water and trapped by circular polarised trap. (b) Collected power spectrum from rotating vaterite, peaks in the power spectrum appear at integer multiples of the rotational frequency ( $f_{rot} \approx 49.8$  Hz)

a long range ordering. There are three main types of liquid crystal transition methods: thermotropic crystals will transition to their liquid crystal phase when sufficiently heated; Lyotropic materials can undergo this transition due to changes in temperature and concentration; and lastly Metallotropic materials - which are composed of both organic and inorganic molecules - change phase according to the ratio of organic to inorganic molecules present. Liquid crystal rotors are rather simple in their production, 4-Heptyl-4-biphenylcarbonitrile (7CB) was purchased from Sigma Aldrich and a small amount was added to a vial of distilled water. The solution was then heated in a water bath to 25° in order to transition the solid crystal into its liquid crystal state. The individual droplets are inherently birefringent and rotate in a circularly polarised trap.

The liquid crystal droplets had a much faster rotation rate than comparable vaterite spheres, due to their higher degree of birefringence and the fact that the droplets are

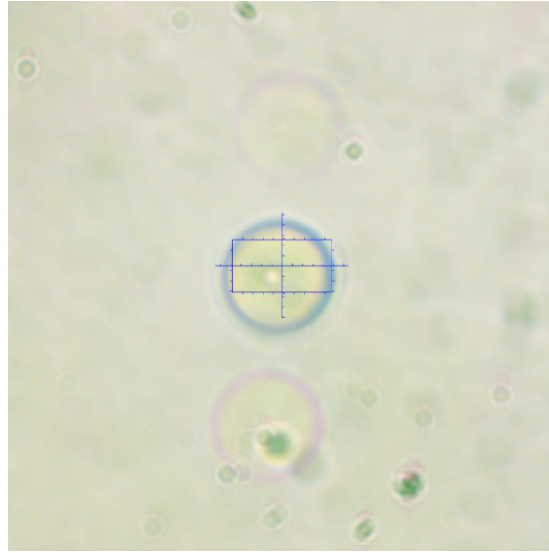


Figure 3.4: Liquid crystal undergoing rotation due to the circularly polarised trap.

far closer to perfect spheres making angular momentum transfer more efficient.

### 3.3.1 Rotation of birefringent micro spheres

Optical tweezing has often been used for micro-rheology, by computing the exact forces being exerted on the trapped sphere, one can determine the local temperature/viscosity of the medium [61, 62]. Using a birefringent particle and rotating it within the fluid, the maximum rotation rate is due to the fluid drag resisting the torque of the trapping beam [62]. If you want to measure fluid flow you can instead use a micro-rotor to see how fluid flow propagates in the medium [63]. Likewise, one can use a galvanometric mirror to probe the drag force of the fluid, by understanding the trap strength (calibrating using a low frequency signal) one can measure the drag force experienced by the local fluid [64]. I

Understanding the fluid velocity around our trapped object is determined mostly by the Reynold's number of our system, for a sphere submersed in a moving fluid of

velocity  $U$  this is given by:

$$Re = \frac{\rho U D}{\mu} \quad (3.2)$$

Where  $D$  is the sphere's diameter, and  $\rho$  and  $\mu$  are the fluid's density and viscosity respectively. In our case we do not have a fluid moving around a sphere but a sphere moving through the fluid at some velocity  $U$ , assuming a no-slip boundary condition we can model the fluid velocity profile based on the velocity of the particle. There are two possible avenues for generating shear flow with a trapped particle; rotation of birefringent particles, and fluid flow induced by particle motion.

Rotating birefringent particles are by far the most common method for generating and measuring fluid flow in a solution. To see if we can even achieve the theoretical maximum shear rate, vaterite spheres were synthesised (see Sec.3.3) submerged in water and trapped with the 1064 nm laser at set to 450 mW. The rotation frequency was determined using the QPD, and the particle sizes were computed by image analysis. With the particle size and rotation frequency, the tangential rotation speed is calculated via:

$$u(r) = \frac{\pi d^3}{4 r^2} \omega \quad (3.3)$$

Where  $d$  is the particle diameter,  $\omega$  is the rotation frequency reported by the QPD, and  $r$  is the distance from the particle's centre. Using Eq.3.3 we computed the fluid flow radiating outward from the centre of the sphere. The shear rate can then be computed

as the partial derivative fluid flow (assuming shearing is generated purely by the flow field):

$$\dot{\gamma}(r) = \left| \frac{\delta u(r)}{\delta r} \right| = \frac{\pi}{2} \frac{d^3}{r^3} \omega \quad (3.4)$$

First we tested the rotational behaviour of vaterite in distilled water, samples of vaterite where diluted down and  $200\mu L$  was pipetted onto the sample stage. Due to Van der Waal's forces some of the microspheres were stuck together, fortunately individual sphere's were still present. Over the course of a few weeks multiple sphere's where trapped and their rotation speeds were measured via the QPD.

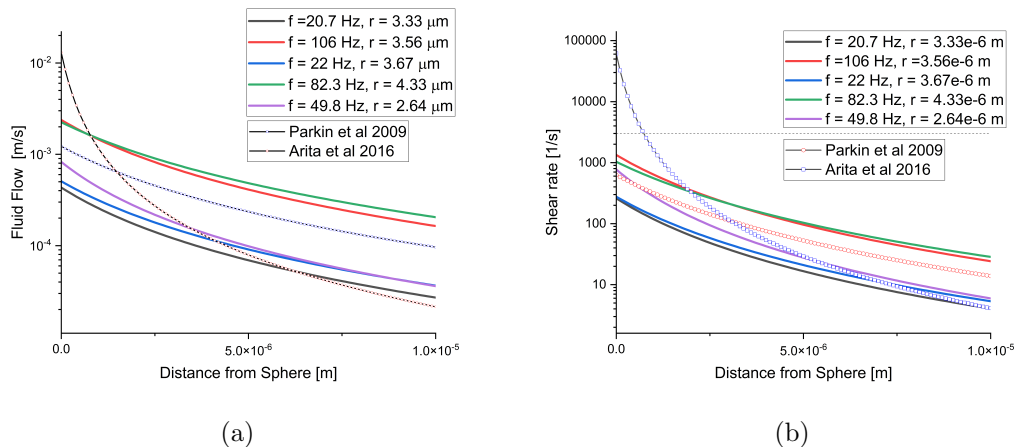


Figure 3.5: (a) Fluid flow radiating out from the surface of a rotating vaterite sphere. (b) Shear rates computed using Eq.3.4, optimal shear rate is of  $3000\text{s}^{-1}$  is indicated by the dotted line. Vaterite radii and rotation frequencies are shown, the laser power was kept constant at 450 mW. Reported rotation rates, and their corresponding fluid flow and shear rates, for vaterite are also plotted alongside lab results.

From Fig.?? there is not a strong relationship between particle size and rotation rate, this is contrary to much of the theoretical predictions that predict an exponential decay with particle size. This can be in part due to the fact that synthesising perfectly

spherical spheres that have uniform birefringence is difficult over multiple experiments and tests. Despite our best efforts at controlling the growth rate the vaterite spheres would often combine together while suspended in water after a short period of time. The fastest reported rotation rate found during this PhD was by [65] that achieved a rotation rate of  $5\text{ kHz}$ , this is plotted on Fig ?? as the dotted line. Even at that extreme a rotation rate the region in which nucleation is at its optimal likelihood is only  $20\text{ nm}$  wide meaning that localising nucleation around a rotating sphere is vanishingly small.

### 3.4 Rotation of micro-rotors in supersaturated solutions

Vaterite samples were synthesised according to [59,66] (see sec. 3.3), and then suspended in distilled water, at the same time a supersaturated solution of Glycine and water was prepared and  $50\text{ }\mu\text{L}$  was pipetted onto a glass cover slip. A single microsphere the vaterite was trapped in a circularly polarised light and brought close to the droplet edge.

After a period of ten minutes if no nucleation event was observed the particle was released and another particle was trapped. Due to the increased viscosity of the supersaturated solution and the proximity to the droplet edge, as previous works have only seen nucleation near the solution-air interface [67–69], the observed rotation rate was rather low or non-existent, the results are tabulated below:

The calculations from fig.?? indicate that even in pure water the rotational speed achieved by a microsphere is insufficient to achieve a significant shear rate more than

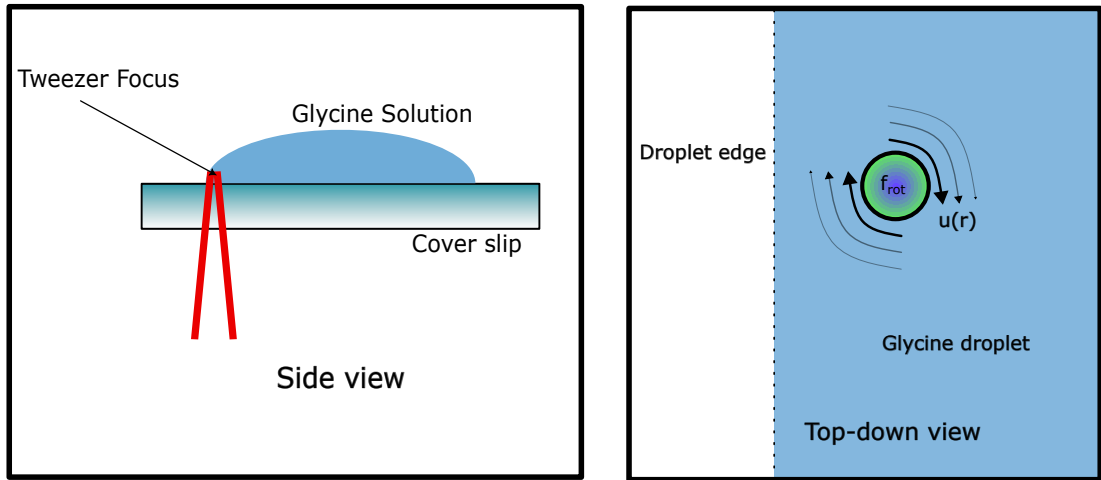


Figure 3.6: Diagram of optical trapping set up for rotating birefringent particles in a supersaturated solution. Left: side view of the trapping set up showing the location of the trap focus at the edge of the droplet of a supersaturated solution. Right: top down view of the glycine droplet with a trapped birefringent particle shown close to edge of the trap. As the particle rotates the drag force from the surrounding fluid generates a flow field around itself (see Eq. 3.3).

Table 3.1: Results from rotating vaterite within supersaturated solution of  $H_2O$  and Glycine. Solubility concentration for Glycine at  $16^\circ$  was  $C^* = 0.2016\text{g/g}$

Super Saturation	Particle radius [ $\mu$ ]	$\omega$ [Hz]	Nucleation [✓/✗]
1.01	2.34	20.7	✗
	5.67	23.3	✗
	3.26	15.4	✗
1.14	1.89	1.23	✗
	3.75	3.54	✗
	4.35	4.86	✗
1.4	3.47	0.00	✗
	1.59	0.00	✗
	6.24	0.00	✗
1.45	6.32	0.00	✗
	3.68	0.00	✗
	5.43	0.00	✗
1.49	4.76	0.00	✗
	7.27	0.00	✗
	1.52	0.00	✗

a few tenths of a microns from its surface. The closest we could trap a microsphere to the droplet edge was in the range of  $5 - 10\mu\text{m}$ , at that distance the fluid flow would

be so low that not even using a liquid droplet rotor would achieve the rotational speeds necessary to localise nucleation. While in theory a sufficiently focused laser could rotate any microsphere to a fast enough to match the speeds expected by [12] the localised intensity would be so large that even using  $D_2O$  would see a significant increase in temperature.

### 3.5 Shearing via a Galvano-mirror

Rather than utilising birefringence rotation, which is subject to issues during synthesis and achieving an ideal particle size, a galvano-mirror was installed to induce controlled particle motion. While typically galvano and gimble mirrors are used to trap multiple particles in a regular pattern, in a sufficiently dilute solution a single silica micro sphere can be moved quickly through a fluid along a preset path. Calculating the shear rate around an individual particle is difficult to do precisely but for low Reynolds numbers we can get an adequate approximation.

For a simple circular path one can estimate the sphere's speed by the radius of its path and the frequency of its orbit  $U = R\omega$ ; however for a more complex path, such as an elliptical orbit the curve needs to be parametrised. One can describe the position parameter of an ellipse as such:

$$r(u) = [a\cos(2\pi u), b\sin(2\pi u), 0] \quad (3.5)$$

where  $a$  and  $b$  are the different characteristic radii of an ellipse, if we say that  $u$

describes time from some initial point we can say  $u = t\omega$  where  $\omega$  is the frequency of orbit. Substituting this in and then taking the partial derivative of position gives:

$$v(t) = \frac{dr(t)}{dt} = [-2\pi a\omega \sin(2\pi t\omega), 2\pi b\omega \cos(2\pi t\omega), 0] \quad (3.6)$$

In order to compute  $U$  we simply take the magnitude of our velocity. For low velocities the fluid flow at the sphere's surface can be computed based on its velocity.

$$u_r(r) = -v(t)\cos(\theta) \left(1 - \frac{3R}{2r} + \frac{R^3}{2r^3}\right) \quad (3.7)$$

Where  $\theta$  is the angle from the direction of movement to the point you wish to measure, and  $r$  is the radial distance to that point. Again taking the partial derivative we can get the shear rate for a particle moving through the fluid:

$$\dot{\gamma}(r) = \left| \frac{\delta u_r(r)}{\delta r} \right| = v(t)\cos(\theta) \left( \frac{3R}{r^2} - \frac{2R^3}{r^4} \right) \quad (3.8)$$

Silica beads ( $r = 1,57\mu m$ ) were trapped and moved along an elliptical path

### 3.6 Nucleation using a moving beam

As mentioned previously, shearing via optical rotation and particle displacement did not result in any localised nucleation events even while in the proximity of the droplet edge.

### Chapter 3. Effects of localised shearing on crystal growth and nucleation

During the experiments with the galvano-mirror, it was found that when no particle was present in the optical trap nucleation events would occur while the beam was close to the edge of the droplet. This has been reported prior, even in undersaturated conditions [70]

## Chapter 4

# Complex Langevin dynamics of spherical dimers

Much of the calibration theory discussed in Chapter 2 assumes that the target particle in question is a single sphere, one who's scattering and motion is easily computed. However, while working with dense colloidal suspensions, one often ends up trapping more than one sphere. Li and Arlt [50] studied the case of two microspheres trapped in a single OT and found that multiple trapped beads could be mistaken for a single trapped bead with altered trap stiffness. Theoretical studies on the case of two trapped microspheres by Xu *et al.* [71] employed a ray-optics based model to show that the two trapped beads are brought into physical contact with each other by optical forces and they also calculated the axial equilibrium positions of the two trapped beads as a function of their size. Experiments in [72] confirmed that the two trapped beads indeed experience different trap stiffnesses in the vicinity of the same potential well. There are further discussions looking into the dynamics of a whole host of asymmetrically shaped

particles [73–75], their results all showing that predicting the behaviour of an arbitrary shaped particle comes with great difficulty due to the fact that the optical force is dependent on a greater number of variables such as orientation and size factors.

In this chapter we consider how the addition of a second sphere into an optical trap can radically effect its dynamics, to the extent that one can no longer rely on typical calibration techniques to characterise the interactions.

## 4.1 Positional and Orientational dependence of Trapping forces

If we wanted to start from first principles and determine the trap strength on our target particle the first step would be to locate the harmonic traps relative to the trap focus. The methodology for computing optical forces has been covered extensively for a number of different trapping conditions [76], so it is relatively easy to compute the trapping force and determine where a simple sphere would be located relative to focal point of the laser. We can do so because the optical force is only dependent on the particle’s relative position. If we instead consider an asymmetric dimer for example we see just by inverting the particle then a secondary harmonic trap can be found below the focus.

We can see that the trap below the focus is comparable in strength to above the focus, however the difference in the transverse strength is far more noticeable. As shown below in Fig ??, the dimer’s orientation and relative position significantly changes the force curve; not only is the trap wider when inverted but the trap stiffness is increased.

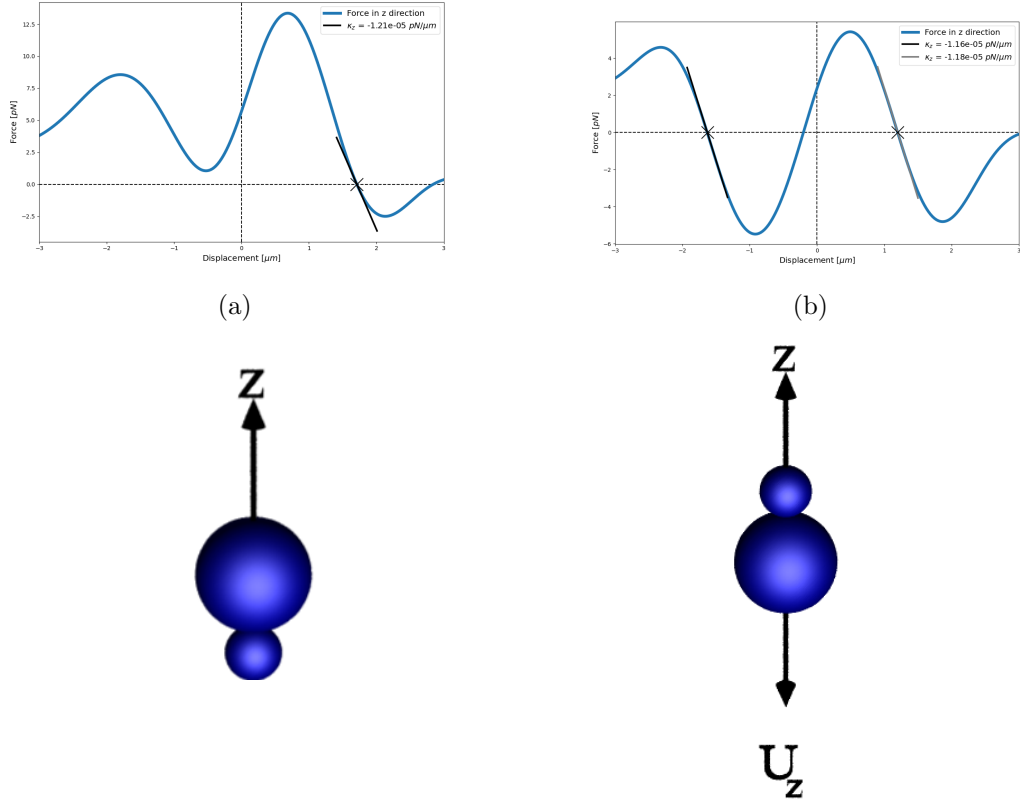


Figure 4.1: Plots of force vs displacement of the point of the contact of the spheres ( $\mu\text{m}$ ) for the case of a dimer of size ratio 2. (a) is the case where the smaller sphere is orientated with the beam propagation direction. (b) is the inverted case, smaller sphere oriented against the propagation direction. Renders to visualise the dimer orientation are shown below each plot. The black lines on each force-curve is a linear fit with the slope being reported as the trap stiffness in the legend.

This highlights one of the challenges involved with studying asymmetric particles, even though its a simple enough process to trap them they maybe characterised very differently depending on their relative position and orientation towards the trap. This can have a significant impact on rheological studies - or attempting to probe any local property - as the variance in trap strength can result in large errors over repeated measurements.

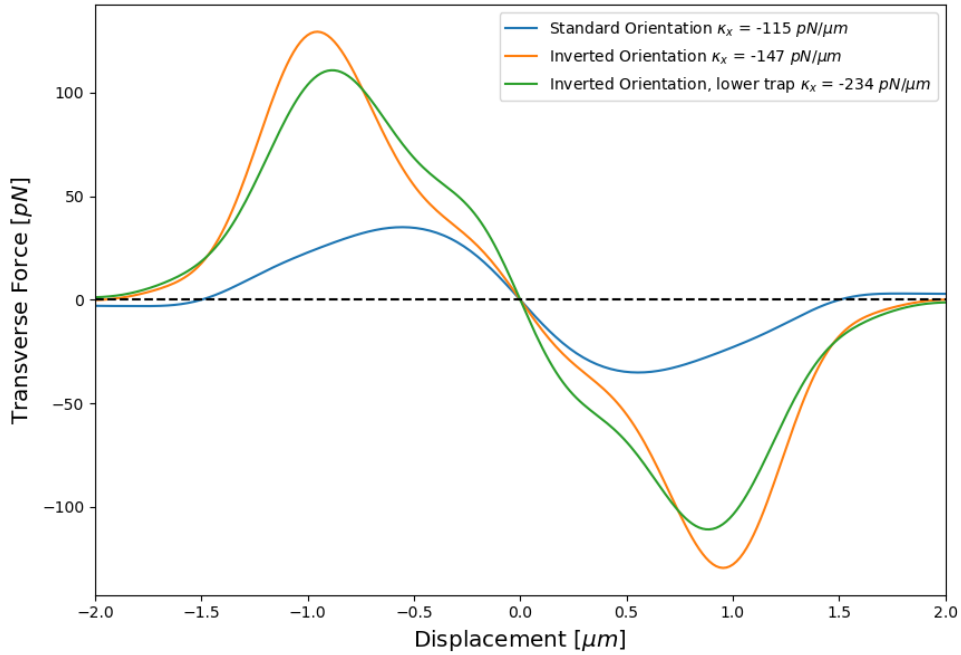


Figure 4.2: Plots of force vs displacement of the point of the contact of the spheres ( $\mu\text{m}$ ) for the case of a dimer of size ratio 2 while being displaced in the transverse plane. With the blue curve representing the force response for a dimer in its standard orientation, orange being the inverted case, and green the same case but placed below the focus.

For completeness the harmonic traps were located for dimers across a range of size ratios - from  $a_1/a_2 = 1$  to  $a_1/a_2 = 10$  - while also recording the trap stiffness for each trap. As  $a_2$  decrease the dimer begins to approximate a single homogenous sphere - at least in terms of location and trap strength. However, for intermediate sized dimers (between  $a_1/a_2 = 1.1$  to  $a_1/a_2 = 4$ ), a second harmonic trap appeared below the trapping focus. Previous work using the ray-optics model have confirmed even in the case that two spheres begin separated the electric field will align the molecules as such that they make contact and are trapped together about a single trapping position [71]. Furthermore it has been shown through proper manipulation of the Gaussian or Bessel

beam modes that any number of trapping potentials can be developed [77]. This result however, is the first example of an orientation dependent trapping situation using only a  $TEM_00$  beam.

#### 4.1.1 Non-trivial harmonic traps

Computing the equilibrium positions when a dimer is aligned with the electric field is relatively simple as the orientational torque is minimised (see Eq.4.1), meaning once trapped the dimer is unlikely to change orientation enough to escape the trap. However, that does not rule out the possibility that there is a stable orientation that is not strictly vertical, in fact most experimental work with symmetric dimers will trap them lying perpendicular to the beam direction [24]. Unlike before where we can simply find the trap by varying the dimer's vertical position its instead more prudent to run a multitude of smaller simulations at a variety of starting positions and orientations. An example for a dimer of size ratio 2 is shown below:

Interestingly while the trap strength of these off-axis traps are similar in magnitude to the vertically aligned dimers, but when the laser power is lowered (around 5 mW) the traps become metastable resulting in the dimer escaping from after some random time while within the trap. If the overall potential depth could be characterised then dimers placed into this orientation could be used as a micro-scale temperature alarm, where by fine tuning of the dimer's parameters would allow you to construct a potential well that can only be escaped when the local fluid temperature exceeds a certain maximum value.

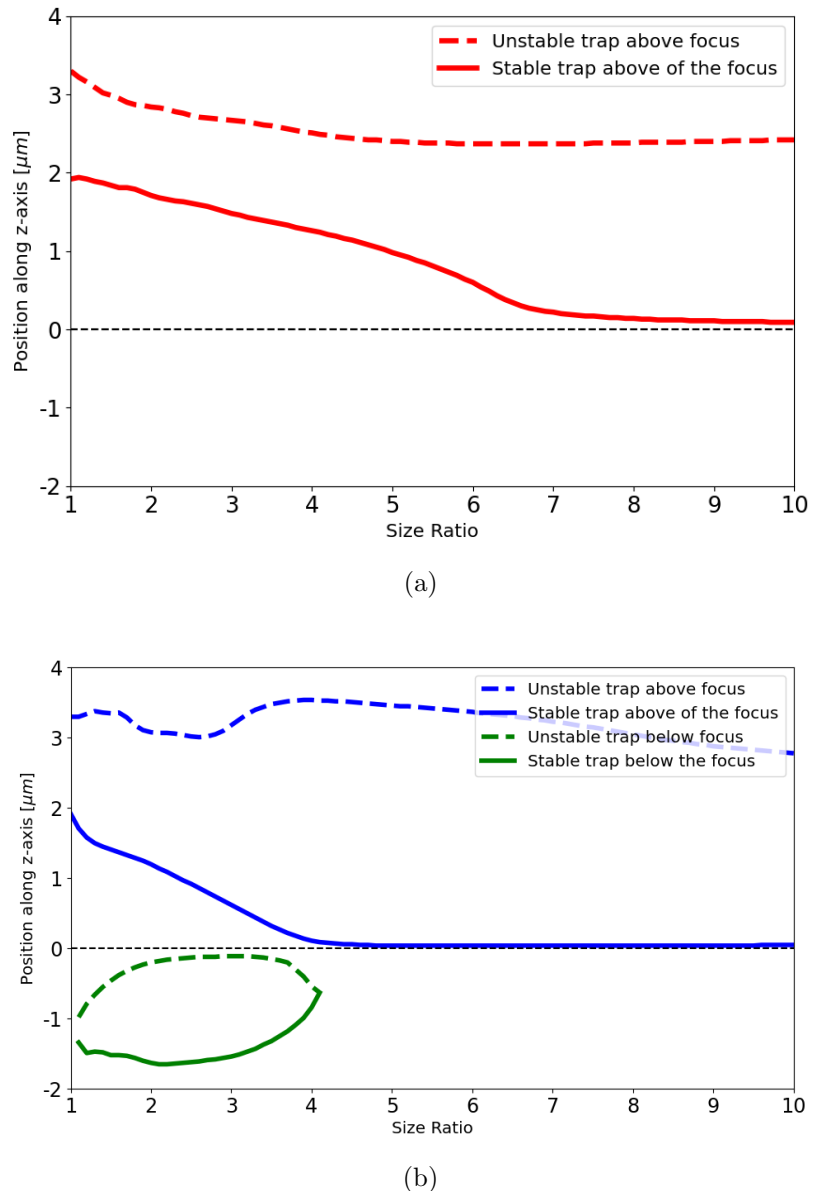


Figure 4.3: Equilibrium positions of optically trapped dimers with varying size ratio, dotted lines represent unstable traps whereas solid lines represent stable trapping positions. (a) shows that dimers with their smaller sphere orientated away from the focus have an expected single trapping position. (b) shows that when the same dimer is inverted 180° there are now stable traps along the beam axis, one below the focus and one above the focus.

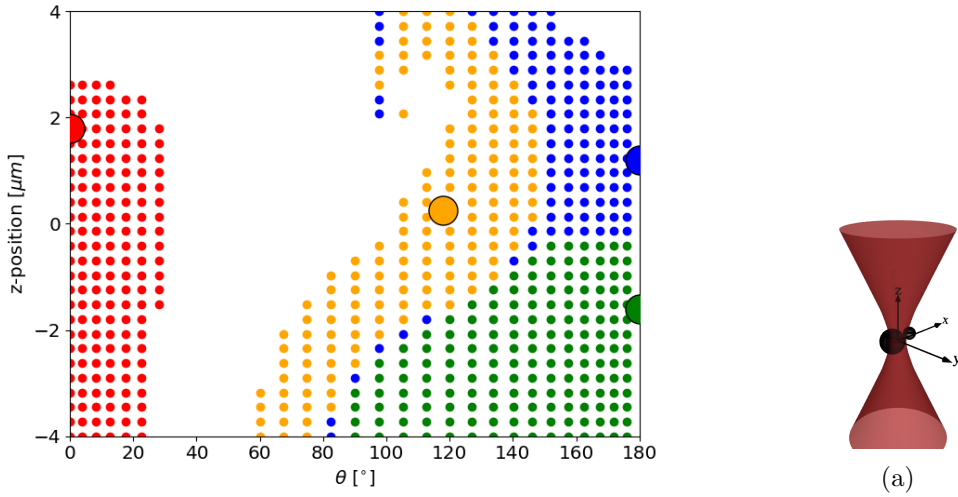


Figure 4.4: Trajectory map of simulations ran using a dimer of size ratio 2 with a laser power of 500 mW. The stable points are indicated by the larger spheres and the starting conditions are colour coded to match the stable point they end up in. Right hand render shows a dimer in its off-axis configuration

## 4.2 Continuous rotational motion due to second-order scattering

One aspect that has yet to be covered in depth with regards to spherical aggregates of any construction is their interaction with circularly polarised light. While most homogenous objects are trapped no differently in different polarisations, dimers have been shown to experience an optical torque [24, 49, 78]. Typically the spin density of an electric field cannot be reduced in homogenous medium due to the fact that the spin angular momentum is conserved locally. In which case the only way to transfer angular momentum to use an object that is anisotropic. This is seen most clearly with birefringent materials, due to fact that the crystal lattice itself is anisotropic, a circularly polarised beam will transfer an optical torque that is proportional to the

difference in the refractive index of the particle. The optical torque is given as:

$$\tau_{opt} = \frac{\epsilon}{2\omega_{laser}} E_0^2 (1 - \cos(kd(\Delta n)) \sin 2\phi) \quad (4.1)$$

Where  $\Delta n$  is the difference in refractive indices of the particle, and  $\phi$  indicates the phase shift in the electric field (for circular polarised light  $\phi = \pi/4$ ). The optical rotation seen with dimers can be attributed to the polarisation of the trapping beam as taking a Fourier transform of the transverse components of the dimers orientation time series reveals a clean rotation rate.

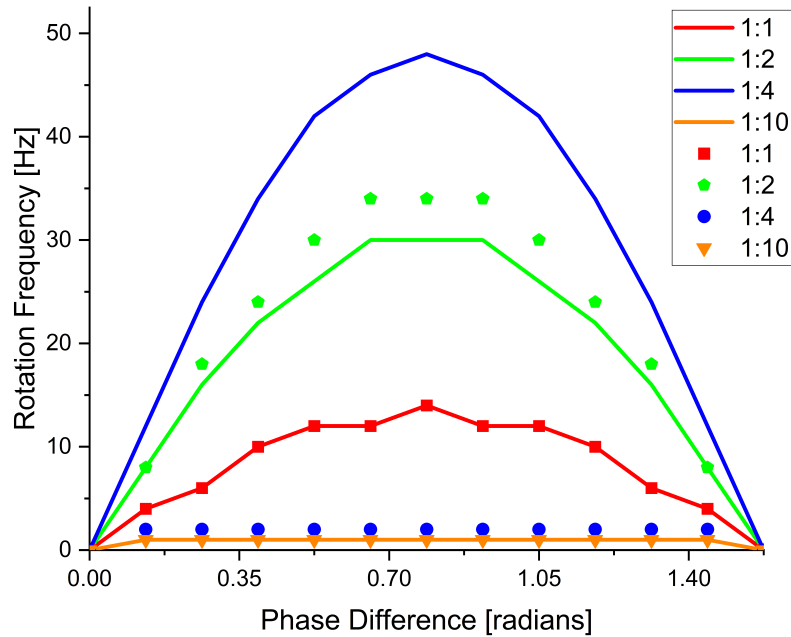


Figure 4.5: Rotation frequency vs component phase difference for differently sized dimers. The solid lines represent the rotation rate experienced while the dimer is in its standard orientation, whereas the solid points are for the case where the orientation is inverted. Laser power = 100 mW

A possible explanation of this phenomena was devised by [79], who found that

highly focused Gaussian beams could produce second order effects in the Rayleigh regime resulting in a photo-kinetic force that results in orbital motion about the beam's central axis. This effect is rather minimal for single sphere's, resulting in a orbital frequency on the order of  $10^{-1}$  Hz, with an order of magnitude difference when trapping aggregates of spheres. They computed the circulation rate by computing the time-average probability flux; however, when extended to the Mie regime we see a completely different behaviour, instead experiencing an optical torque about their long axis.<sup>S</sup> This rotation was first noted by Vigilante and co-workers who only considered this behaviour for a symmetric dimer [49]; we run number of simulations for differently sized dimers in a circularly polarised trap and looked at the rotation rate. We found that not only is the rotation rate dependent on the size of the dimer, but also on its orientation and therefore their axial position.

It is difficult to see from the graph, but the rotation rate never truly goes down to zero, reaching a minimum of 2 Hz, which would imply that a second sphere of radius 200 nm is enough to induce rotational motion. We used *mstm* to look at the stokes parameters from the scattered field from a simple plane wave incident on our dimer, the proportion of circularly polarised light is minimal compared to the proportion of plane polarised light, which indicates that this rotational motion is not due to any inhomogeneity in the dimer that might impart angular momentum to the scattered beam - as compared to a anisotropic scatterer like vaterite.

These results are somewhat contrary to other work with silica dimers [12, 24, 78]; previous experiments have trapped the dimer in an orientation perpendicular to the beam propagation direction. The rotational motion is induced due to the asymmetric

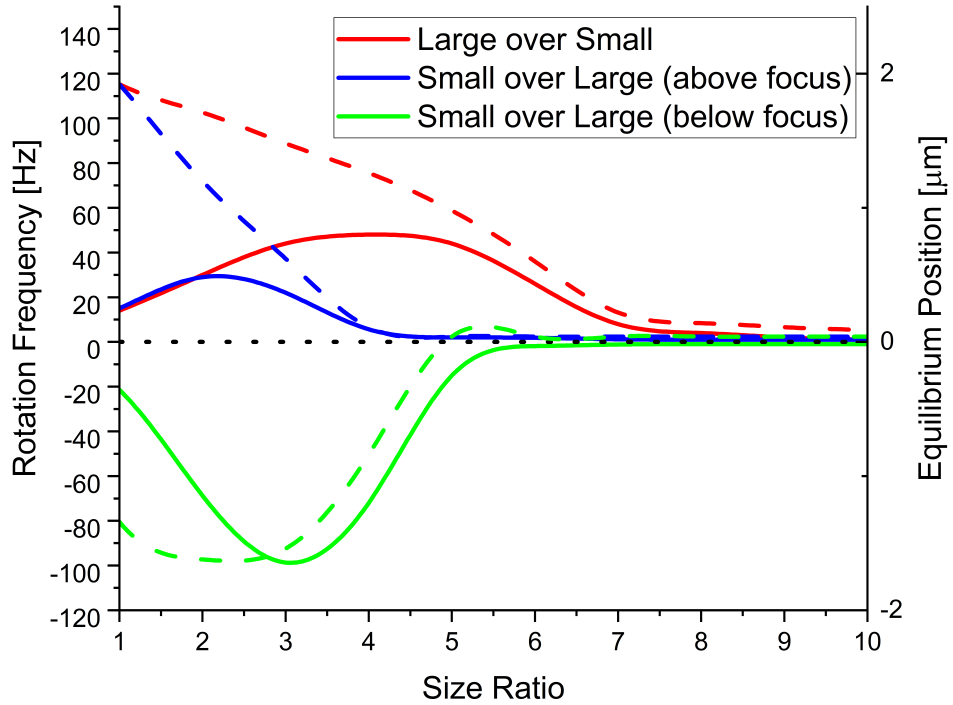


Figure 4.6: Rotation rate plotted against dimer size ratio for a variety of different simulation scenarios. The red line is for the case where the larger sphere is above the smaller sphere. The blue line is the inverted case, while the initial position is above the focus of the trap. And lastly the green line is again for the inverted case, but when the dimer's initial position is below the focus of the trap.

geometry creating an unbalanced polarisation susceptibility along its long axis as compared to its short axis; therefore its long axis is aligned with the polarisation vector and can rotate freely [24]. This however cannot be the case with our simulations as the dimer rotates about its long axis, meaning there cannot be an asymmetric axis to align with the beam's polarisation vector. Furthermore, we see a non-linear increase in the rotational speed of our dimers with size, the drag torque from the surrounding fluid is  $\propto r^3$  so the expectation is that the rotation frequency should fall off with increasing size. This indicates that the rotational motion is due to the shape asymmetry

#### Chapter 4. Complex Langevin dynamics of spherical dimers

of the dimer and not solely due to the beam's angular momentum. Measurement of this photo-kinetic force is difficult to achieve due to the fact that previous analysis was conducted in the Rayleigh regime, where the polarizability of our dimer can be approximated as:

$$\mathbf{p}(\mathbf{r}, t) = \alpha_x E_x(\mathbf{r}, t) \hat{\mathbf{e}}_x + \alpha_y E_y(\mathbf{r}, t) \hat{\mathbf{e}}_y + \alpha_z E_z(\mathbf{r}, t) \hat{\mathbf{e}}_z \quad (4.2)$$

where the polarizability is given as a 3D vector for the three principle Cartesian directions. In order to measure the magnitude of second order contributions we would need to construct a dipole array that fully captures the scattering of a dimer. Measuring the optical torque makes it clear that the polarizability is a contributing factor to this optical rotation phenomena. Rotating a symmetric dimer in the  $x-z$  plane reveals that while the dimer can be rotated in an orientation perpendicular to the beam rotational torque is maximised when rotated while aligned with the optical axis.

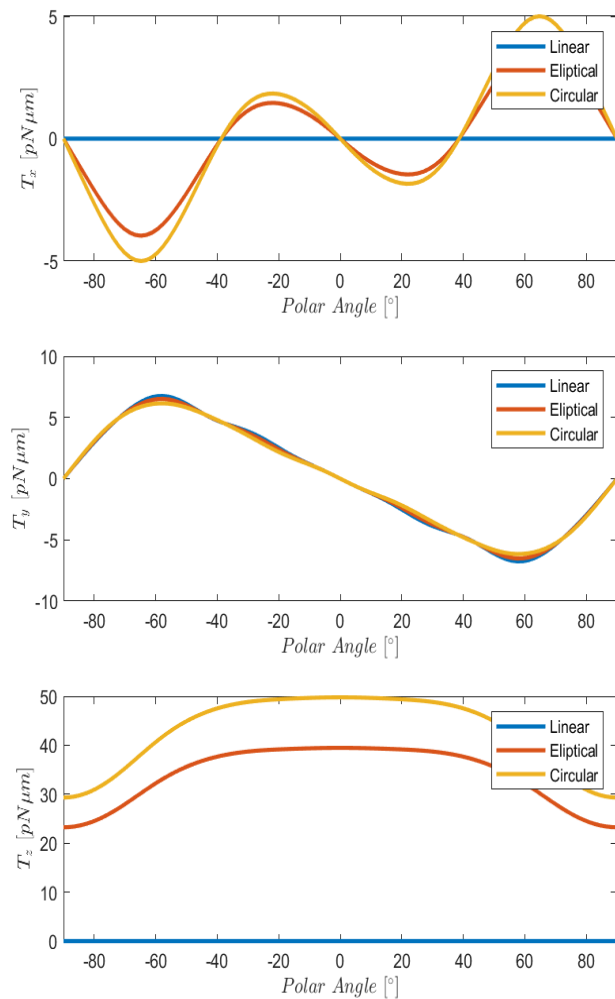


Figure 4.7: Optical torque against polar angle  $\theta$  about the three primary axis (top: torque about the x-axis; middle: torque about the y-axis; bottom: torque about the z-axis) on a symmetric dimer in linear, elliptical, and circular polarisation beams. Diagram to the right is for visual clarity about the direction of  $\theta$ .

### 4.2.1 Gyroscopic Precession using asymmetric dimers

As mentioned in section 4.1.1 for specificity sized dimers there is the potential for non-vertical trapping orientations in which the dimer is located in a harmonic trap. When trapped by a circularly polarised light these dimers exhibit gyroscopic precession. As shown in fig ?? the dimer's is rotating about it's long axis (as seen by the periodic behaviour of  $u_x$  and  $u_y$ ), while also precessing around the optical axis of the beam, resulting in a second order oscillation in  $s_z$ .

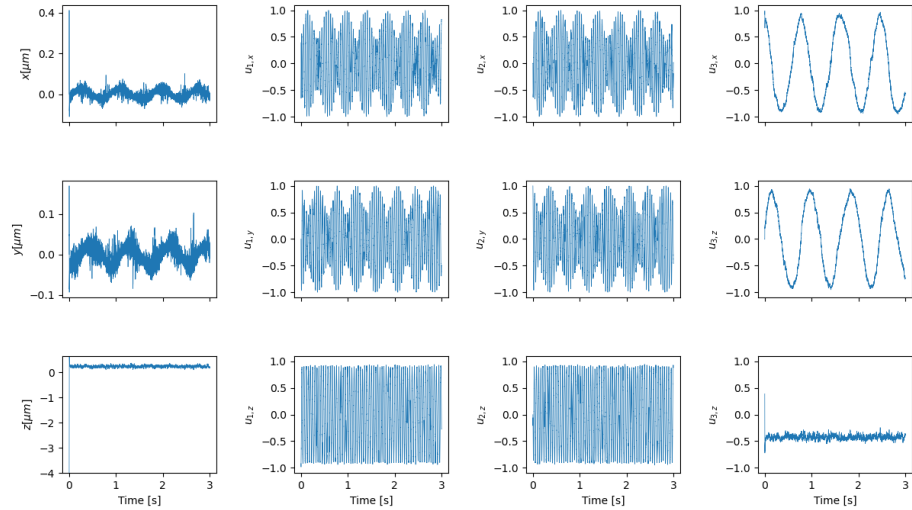


Figure 4.8: 3 second trajectory of a dimer trapped in an off axis orientation, laser power was set to 100 mW. The far left column depicts the dimer's centre of mass position with time; middle two columns are the  $x$ ,  $y$ , and  $z$  components of the vectors  $u_x$  and  $u_y$ ; last column depicts the components of the vector  $u_z$  which defines the dimer's orientation.

Applying a Fourier analysis to the above trajectory reveals the 3 fundamental frequencies typically associated with precession; the  $u_{z,1}$  and  $x(t)$  series show a precession frequency of  $1.33 \text{ Hz}$  whereas the series  $u_{x,1}$  and  $u_{y,1}$  show a combined periodic signal - a rotational frequency of  $23 \text{ Hz}$  and a nutation frequency of  $20 \text{ Hz}$ . Previous stud-

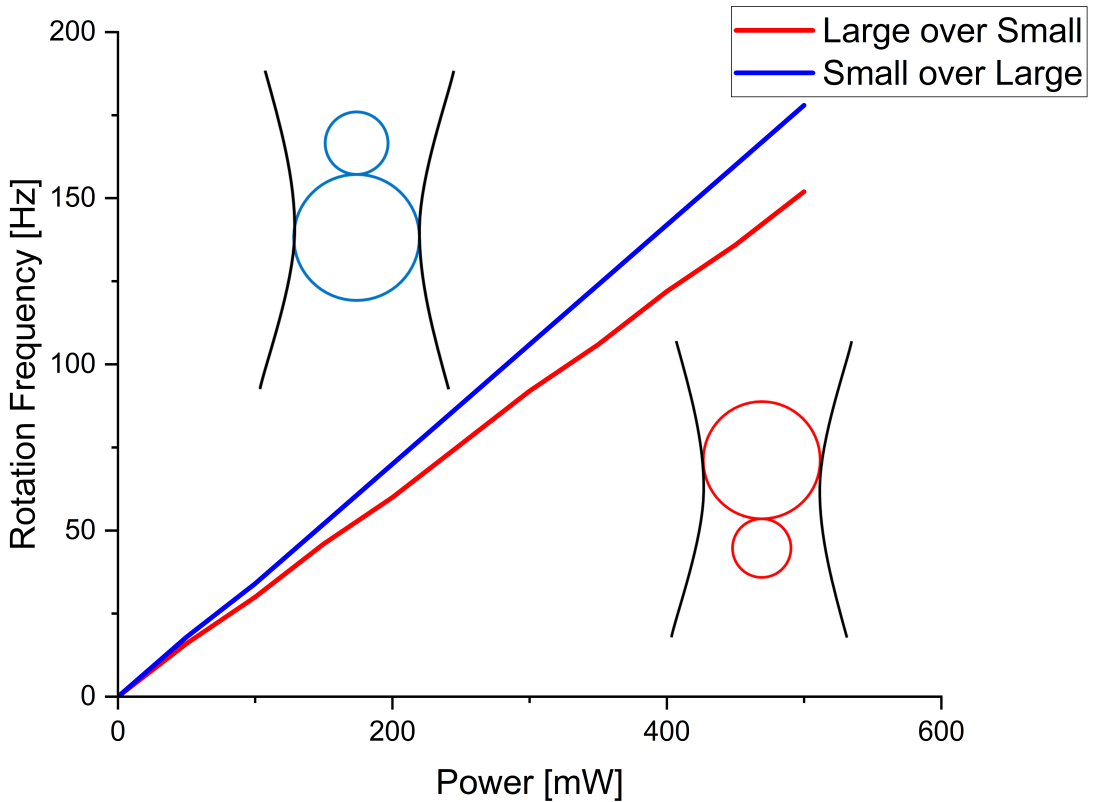


Figure 4.9: Rotational frequency vs laser power for a dimer in both vertical orientations.

ies into amorphous silica nanoparticles found a linear relationship with the rotational frequency and the laser power, but no such relationship existed with the precession frequency. Our own results shows a similar linear relationship with vertically aligned dimers.

The linear relationship could partly be due to fact that we do not account for the change in viscous forces with increasing laser power. It is far more likely that the rotational frequency reaches a maximum value assuming that the bulk fluid can readily absorb the laser.

This gyroscopic motion has been demonstrated previously in nanoparticles [80–83] but has not been observed for micron scale aggregates. Since the torque is computed by

evaluating the beam coefficients it is difficult to apply this result to micro-rheology experiments as one would need to know the exact magnitude of the optical torque ahead of time in order to make estimations about the local fluid viscosity. This is trivial for a birefringent spherical particle, less so for spherical aggregates whose equilibrium position and orientation are unknown.

### 4.3 Characterisation of asymmetric dimers via PSD analysis

As discussed in 2.6.1, one of the methods developed to work in conjunction with [49] is a simulated quadrant photo diode for as a position detection system. While it is possible to extract all of the relevant dynamical information from a simulation, confirming the same behaviour in an experimental setting can be challenging.

As a benchmark we start by considering a single sphere within an optical trap. After a 3 second trajectory (the typical time necessary to collect a power spectrum) the sphere's power spectra was recorded and a fitted to eq. 2.45.

As shown in fig. ??, the two power spectra report different corner frequencies which would indicate that the trap is not perfectly circular. Using *ott* we can compare the expected trap strength to what is reported by a quadrant photo diode:

Fitting parameter	<i>ott</i> estimates		QPD fitting		Simulation fitting	
$f_c$ [Hz]	447	450	439	474	523	513
$\kappa$ [ $pN/\mu m$ ]	53.05	53.40	51.96	56.09	61.94	60.7
Ellipticity	8.16 %		27.17 %		13.8 %	

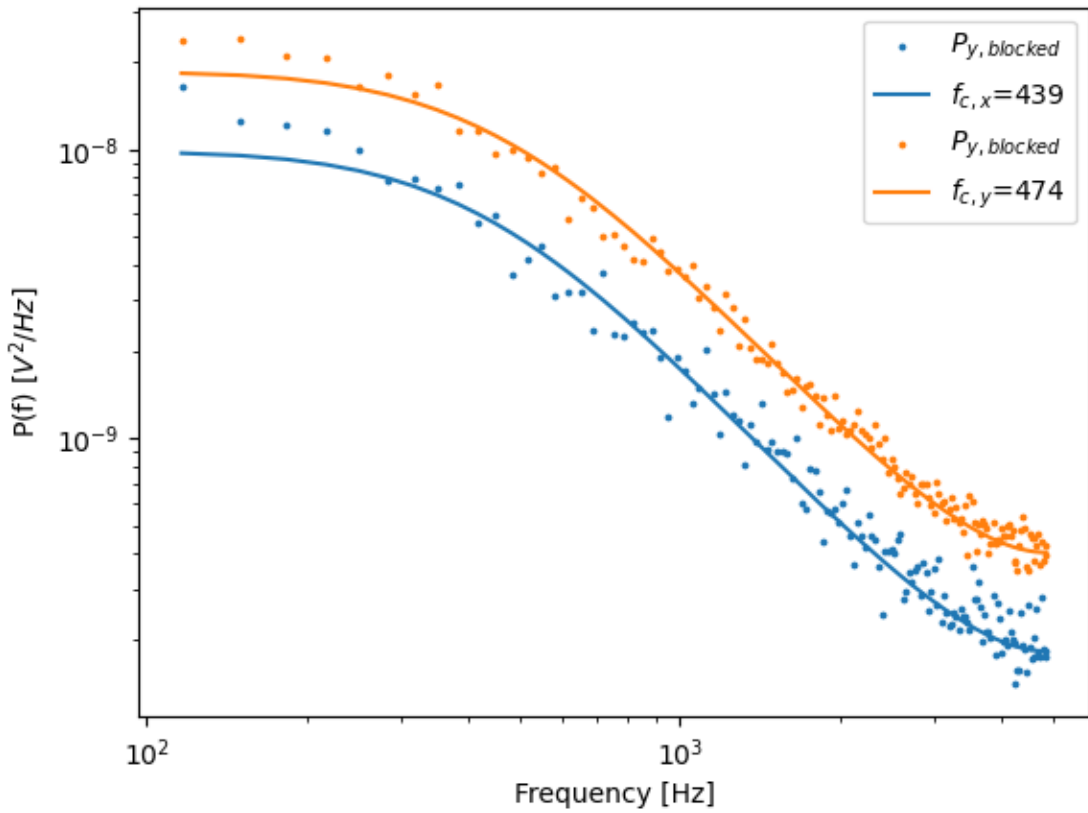


Figure 4.10: Recorded power spectra fitted to eq. 2.45, scattered points represents the blocked data ( $n_b = 100$ ). Corner frequency for the Lorentzian curves are reported in the legend.

Where the ellipticity of the beam is given by  $e = (1 - \kappa_y/\kappa_x)^{0.5}$  and is a measure of the symmetry of the beam wavefront. Its clear from these initial results that the QPD is more sensitive to changes along the y-axis than the x-axis when compared to the direct *ott* calculations. Typically, even an industrial Gaussian beam will produce an elliptical diffraction limit spot when heavily focused; in their tutorial for optimizing the PSD analysis, Berg and Sorensen reported a ellipticity of around 15 % after a total calibration time of 81 seconds [47]. The reason for this discrepancy can be explained partly by the fact that our estimation of the trap geometry via *ott* is based on the

force-displacement curve while the sphere is moving in only one direction, whereas the QPD is estimating the trap geometry by extrapolating from far field scattering signals. We now consider a symmetric dimer in identical simulative conditions.

Fitting parameter	<i>ott</i> estimate		QPD fitting		Simulation fitting	
$f_c$ [Hz]	409	334	431	424	274	285
$\kappa$ [ $pN/\mu m$ ]	48.51	39.58	51.13	50.26	32.45	33.75
Ellipticity	42.8 %		12.7 %		13.8 %	

Now we see that the *ott* predicts a more elliptical trap compared to the QPD model which says the trap is far more symmetrical while trapping a symmetric dimer. A potential reason that *ott* no longer expects a circular trap could be due to how it computes the beam shape coefficients; by point matching in the far field before the focus means a loss in accuracy for objects that trap above the focus. The change in the QPD estimation can be partially explained by the fact that rotational effects are not accounted for in the Lorentzian power spectra, only translational motion. Typically, rotational motion is only ever detected when it is periodic (take for example Fig. ??), when the motion is stochastic the entire power spectra is effected making it near impossible to separate the translational and rotational contributions from a single power spectra.

## 4.4 Conclusions

Considering the simplicity of a scatterer such as a dimer, one would assume that the dynamics of such an object would be relatively easy to predict. Simulations of dimers in the Mie regime show that not only do they have multiple positions and orientations

#### Chapter 4. Complex Langevin dynamics of spherical dimers

in which they can be trapped but also that their interaction with circularly polarised light is heavily dependent on the axial position and trapping orientation. Dimer's have the potential to be used as adaptive micro-rotors, being simple to synthesise and can be made out of any material of choice, but in order for these particles to be used as such one needs a means of characterising the optical torque applied. While estimations can be made in the Rayleigh regime due to the dimer being treated as point dipole, Mie regime micro rotors require an in-depth theoretical description of the mechanism that is creating this optical torque.

## Chapter 5

# Detection and Characterisation of rotational spherical aggregate rotational dynamics

### 5.1 Simulative QPD

A QPD is simply a measure of the total electric field incident on a photo diode, in order to accurately simulate a QPD response careful consideration of how the Electromagnetic fields are defined is required.

#### 5.1.1 Incident beam

The incident beam is simple enough to define given our set up parameters, for the sake of simplicity we assume that our beam is a Laguerre-Gaussian beam of mode [0.0, 0.0] (which is simply a pure Gaussian beam). \*Ott\* uses a point matching approach to

Chapter 5. Detection and Characterisation of rotational spherical aggregate  
rotational dynamics

approximate the beam shape coefficients of the incident field by fitting it to the far field estimate, the beam is of the form:

$$E_{inc}(kr) = \sum_n^{\infty} \sum_{m=-n}^n a_{mn} Rg M_{nm}(kr) + b_{nm} Rg N_{nm}(kr) \quad (5.1)$$

Where  $RgM_{nm}(kr)$  &  $RgN_{nm}(kr)$  are regular vector spherical wave functions, \*ott\* allows us to change the basis of the the incident beam to suit our needs, because we are measuring in the far field we want to set our incident beam to be an outgoing spherical wave so that we can compute the intensity on the QPD. For spherical waves the field can either be expressed as an incoming/outgoing wave (with a singularity at the origin) or as a regular wave around the origin; for incoming/outgoing waves the wave functions use the first/second forms of the Hankel function respectfully. In order to compute the regular spherical wave at the origin we replace the Hankel function with the Bessel function which is simply the average of the first and second forms of the Hankel function, so at the origin we avoid a singularity of the EM field.

We can if we want further restrict the incident beam by applying setting the truncation angle to match our microscope object, this essentially applies a cut off point to the In order to compute the scattering from the target particle \*ott\* uses the t-matrix method, this is not essential for a simple sphere but is far more important for complex shaped particles such as our dimers. If the T-matrix is loaded in from \*mstm\* we need to convert the \*mstm\* t-matrix to a form more suitable for \*ott\*:

$$\begin{pmatrix} p_{nm} \\ q_{nm} \end{pmatrix} = T \begin{pmatrix} a_{nm} \\ b_{nm} \end{pmatrix} = \begin{pmatrix} aT_{nm}^{TM} & aT_{nm}^{TE} \\ bT_{nm}^{TM} & bT_{nm}^{TE} \end{pmatrix} \begin{pmatrix} a_{nm} \\ b_{nm} \end{pmatrix} \quad (5.2)$$

For \*mstm\* the T-matrix is packed as a column vector:

$$T_{MSTM} = \begin{bmatrix} aT_{n,-n}^{TE} & bT_{n,-n}^{TE} \\ aT_{n,-n+1}^{TE} & bT_{n,-n+1}^{TE} \\ \cdots & \cdots \\ aT_{n,n}^{TE} & bT_{n,n}^{TE} \\ \hline bT_{n,-n}^{TM} & bT_{n,-n}^{TM} \end{bmatrix} \quad (5.3)$$

Where as \*ott\* packs the T-matrix with sub matrices:

$$T_{Ott} = \begin{bmatrix} \begin{pmatrix} aT_{n,-n}^{TM} & aT_{n,-n}^{TE} \\ bT_{n,-n}^{TM} & bT_{n,-n}^{TE} \end{pmatrix} \\ \begin{pmatrix} aT_{n,-n+1}^{TM} & aT_{n,-n+1}^{TE} \\ bT_{n,-n+1}^{TM} & bT_{n,-n+1}^{TE} \end{pmatrix} \\ \cdots \\ \begin{pmatrix} aT_{nm}^{TM} & aT_{nm}^{TE} \\ bT_{nm}^{TM} & bT_{nm}^{TE} \end{pmatrix} \end{bmatrix} \quad (5.4)$$

### 5.1.2 Scattered and Total Fields

With the T-matrix in hand we can compute the scattered beam by multiplying our beam shape coefficients with the T-matrix to get out the scattered field. Now in order to simulate a real QPD we need to account for the motion of our target particle within the trap, taking a typical trajectory file we read off each line in order to translate and rotate the beam. Translation is a rather simple process, simply involving us to shift the beam laterally, small deflections are generally unnoticeable for the incident beam but are much more noticeable in the scattered field (the below figure shows the result of shifting the incident beam  $1\mu m$  to the right):

The QPD does not just pick up the scattered light however, it instead is receiving a combined signal from both the incident field and scattered field simultaneously, as mentioned by [Rohrbach](#) the total intensity can be computed by taking the magnitude of both the incident field \*focused at the origin  $[0, 0, 0]$ \* and the scattered field originating from  $[\delta x, \delta y, \delta z]$  (top left and bottom right plots in the above figure). This means we do not need to worry about any translation effects being 'double-counted' in the QPD's signal as we are only shifting the scattered field meaning the QPD signal is only picking up the interference due to the shifted scattered field. I conducted some unitary tests where I scanned the beam position laterally along the x-axis and measured the QPD's 'x-signal' for x, circular and y-polarized light which yielded the following QPD responses. The target particle was  $1.57 \mu m$  and the scan range is set to  $[-4, 4\mu m]$

Where  $S_x$  is given in blue, and  $S_y$  is given in orange, the plots make it clear that the polarisation of the beam have a minimal effect on the QPD signals if the particle

## Chapter 5. Detection and Characterisation of rotational spherical aggregate rotational dynamics

is traversing in one direction, its clear that the displacement from the beam centre is far more important than the polarization of said beam. This is backed up when we look at [Rohrbach's](#) results, who studied a  $150\text{ nm}$  sphere ( $n = 1.57$ ) submerged in water with a focusing lens of numerical aperture 1.2, and beam power of  $3\text{ mW}$ . The condensing lens' numerical aperture was not set to a particular value and was instead varied between 0.13-1.2, as a compromise we selected a condenser numerical aperture of 0.525, corresponding to a acceptance angle of  $31.6^\circ$ .

Where the points are Rohrbach's results and the solid line's are our QPD's own replication. The dashed horizontal lines on the left represent the maximum displacement in the lateral displacement which is given by the combined beam radius and particle radius (assuming a beam radius of  $0.54\text{ }\mu\text{m}$ ); we can say that any displacements beyond this distance, while non-zero these displacements are unlikely to occur while a particle is trapped at the focus. Whereas the right most plot's dashed horizontal lines represents the Rayleigh range of the Gaussian beam, this represents the transition between plane wave and spherical wave regimes. Interestingly while our results close to Rohrbach's while close to the focus we see it begins to diverge beyond the first peak, this shouldn't be an issue for a typical optical tweezer calibration as we can assume that the maximum displacement will be within this linear regime.

Now the above plots only consider the QPD response to movements along the cartesian axis, however obviously for any Brownian motion the movements are a combination of displacements in each cartesian direction. We might assume naively that any displacement  $\Delta r$  will result in a linear combination of QPD responses; for low precision force measurements this assumption is adequate, however when high precision is re-

## Chapter 5. Detection and Characterisation of rotational spherical aggregate rotational dynamics

quired we find that this assumption is longer adequate due to something referred to as cross-talk. Cross talk arises when movement in one direction results in a QPD response change in the other orthogonal direction, there is no one reason for this effect, it could be a result of differing sensitivity in the photo diodes, it could be because the scattering is slightly asymmetric meaning the scattering falls outside the QPD, or it could be a result of mis-alignment in the set up. This can have unintended effects, for example it may lead to the apparent rise of a curved trajectory rather than a straight path: Consider a particle moving purely along the x-axis, with 0 cross-talk the QPD response should perfectly match the above curve  $S_x(x, 0, z_0)$ , with  $S_y$  being flat in comparison; if however there is cross talk between the channels then  $S_y$  will have some significant non-zero value (or it may even grow with increasing displacement), implying that the particle is actually moving in both the x and y directions simultaneously. First we checked for this by measuring the QPD response for random positions within the XY plane:

Where  $S_x$  is plotted on top and  $S_y$  is plotted below, as shown by the above plot we see that they still possess similar shapes to the previous plots but now with additional noise terms, making it clear that for any trajectory there will be cross talk. This means that trying to get a one-to-one measurement of the particle's displacement is not possible by simply looking at the QPD response, to do that we can need to calibrate the trap.

[Berg and Flyvbjerg](#) have an excellent breakdown for accurately calibrating an optical tweezer, in addition they discuss how to minimise cross-talk effects. For two correlated power spectra, the cross correlation is given as:

$$P_x = |\hat{S}_x(f)|^2 \quad (5.5)$$

$$P_y = |\hat{S}_y(f)|^2 \quad (5.6)$$

$$\rightarrow P_{xy} = \text{Re}(\hat{S}_x \hat{S}_y^*) \quad (5.7)$$

Now if the two directions are correlated then  $|P_{xy}|^2/P_x P_y$  should be non-zero for all frequencies, in order to eliminate cross-talk effects we need to minimise the cross-correlation for all frequencies. They showed that it is possible to find a transformation of the time series  $(x(t), y(t))$  to one that possesses the property that  $P_{x'y'}(f) = 0$  for all frequencies. They found these transformed positions by minimising the sum cross-correlation:

$$\sum \frac{P_{x'y'}}{P_{x'} P_{y'}} = \sum \frac{(1 + bc)P_{xy} + cP_x + bP_y}{(P_x + 2bP_{xy} + b^2 P_y)(P_y + 2cP_{xy} + c^2 P_y)} \quad (5.8)$$

Where b and c are fitting parameters, by minimising this function one can adjust each spectra in order to eliminate cross talk effects and provide a more accurate calibration of the optical trap. Furthermore with the fitting completed, the time series can be then transformed in order to eliminate the cross talk effects:

$$x'(t) = S_x(t) + bS_y(t), \quad y'(t) = S_y(t) + cS_x(t) \quad (5.9)$$

Where  $x'$  and  $y'$  are now uncoupled coordinates that when Fourier transformed provide the uncorrelated power spectrum. With the fitting complete we can now adjust our time series in order to get a replication of the lateral trajectory.

## 5.2 Rotations and Asymmetric particles

Rotational motion is something that is not often necessarily considered when characterising Brownian motion, often because separating the contributions from rotational and translational motion is challenging. Depending on the rotational and translational trap stiffness the collected QPD signal will be aliased and typical calibration techniques cannot characterise the particle and trap interactions. This is often why most of the research into trapping asymmetric objects does not delve into power spectra analysis, as there is no real way of modelling the QPD response from an asymmetric object.

Now for isotropic scatterers any rotation is often not an issue when it comes to QPD analysis, even if a sphere rotates  $180^\circ$  the scattering should be identical (assuming its relative position is the same). Now \*ott\* deals with both translations and rotations by moving the beam itself and computing the scattering from by once again expanding the spherical wave functions, the problem that arises from this is that the portion of the spherical wave that is evaluated by the QPD will pick up said rotation and produce a non-zero signal even if the scatterer in question is isotropic. This means we need to counter rotate the total field prior to collecting the QPD signal, this captures the effects of an anisotropic scatterer but has no effect for an isotropic scatterer. As a test the QPD response from an isotropic sphere of  $1.57 \mu m$  was collected at multiple

Chapter 5. Detection and Characterisation of rotational spherical aggregate  
rotational dynamics

angles, between 0 and  $2\pi$ , then as a comparison a symmetrical and 1:2 dimer were also subjected to the same rotations and their QPD responses evaluated.

Where on the left we have an isotropic sphere, then a symmetrical dimer, and lastly a 1:2 dimer. The left most plot shows that simply using the inverted rotation matrix is sufficient to prevent rotation effects being double counted. For dimers however, rotating about a given axis gives us a clear change in the signal for even a slight rotation about any axis.

### 5.3 Power Spectra of single sphere vs spherical aggregates

In order to verify that the QPD is outputting correct signals we first compared the module to the only other known instance of simulating a QPD response, that being the work of [Rorrbach](#). In their paper they looked at the signal response produced by a single sphere ( $r = 150 \text{ nm}$ ,  $n = 1.57$ ) being scanned along the three Cartesian axis in the proximity of a  $1064 \text{ nm}$  NIR beam with a numerical aperture of 1.2. As shown by fig ?? the two responses are remarkably accurate close to the origin; with only slight deviations as you move past the harmonic region, the difference can be explained due to how the two evaluate the total fields. Where in our case the incident and scattered fields are reduced to 0 at the origin, whereas Rohrbach's work evaluates the fields the fields as being non-zero at all points, as you move beyond the origin this discrepancy grows.

Since we are only interested in the dynamics of spherical aggregates upon reaching equilibrium we do not need to be concerned about the deviation from Rohrbach's results

so long as the particle's displacement does not exceed the linear region at the origin.

The axial response curve is slightly more involved, requiring that the condenser lens numerical aperture is adjusted until a harmonic response curve is achieved [55].

In order to verify that the QPD can accurately capture the dynamics of the target particle we first simulated a single sphere ( $a = 1\mu m$ ,  $n = 1.59$ ) in the focus of a  $1064 nm$  laser. Using *ott* the trap stiffness is computed by applying a linear fit to the force-displacement curve along the x and y axis'; for a linearly polarised trap the gradient force is greater in the polarisation direction than transverse case. We see this reflected in the simulated QPD, the fitted Lorentzian curves have different corner frequencies indicating that the beam's polarisation is influencing the dynamics of the trap.

Next we consider a dimer composed of two sphere's similar to the previous sphere, we again apply the QPD module to reproduce the power spectrum. Previous experimental work found that a pair of trapped beads would half the corner frequency from the reported power spectra. However, in our own simulations we see instead an increase in the expected trapping force from our QPD method, with the maximum trap stiffness expected for a dimer of size ratio 5. Compared to *ott* in which the maximum trapping strength is expected at a size ratio of 2. This can be somewhat explained by the fact that as the second sphere shrinks the centre of diffusion approaches the centre of the larger sphere and thus the dimer's orientational behaviour is similar to a single sphere, only subject to slight Brownian motion. Therefore one should expect that for aggregates containing multiple sized particles (e.g. cellular samples) typical characterisation techniques may over estimate the strength of the trap.

## 5.4 Monitoring Stochastic rotational motion using static light scattering

Orientational dynamics to an anisotropically scattering shape are difficult to characterise due to the coupling of rotational and translational effects. As shown in the previous chapter the dynamics of even simple dimers are heavily dependent on the particle's position and orientation, this is reflected in literature where several engineering solutions have been devised to decouple translational and orientational motion [ , ].

While a majority of latter work has been focused on nano-particles (falling into the Rayleigh Regime) and utilising florescence

### 5.4.1 Coordinate System

In the case of our probe beam the  $+z$  direction points from the surface of the probe directly to the centre of diffusion in our dimer, with the  $+y$  direction pointing towards what would be our trapping beam, and the  $+x$  direction pointing into the page. The origin of our coordinate system is fixed on the centre of the focus of our trapping beam, meaning as our dimer's centre of diffusion moves the origin is kept constant.

### 5.4.2 Dimer

The dimer is defined by two spheres, in the trapping frame this would be orientated by  $s = [0, 0, 1]$  however in our scattering set up this is rotated to  $s = [-1, 0, 0]$  as the large sphere is furthest from the trapping beam. We scale the position of each sphere by the

factor L:

$$L = \frac{1}{k} = \frac{\lambda}{2\pi} \quad (5.10)$$

Where  $\lambda$  is the wavelength of light and is given in nanometres, this means every position must be also provided in nanometres.

### 5.4.3 Beam

Our probe beam is rather simple to define, we firstly say that the probe is a plane wave by setting the Gaussian beam parameter  $C_B$  to 0. We also say the beam is un-polarized by defining the Stokes vector as [1, 0, 0, 0].

### 5.4.4 Detectors and Pixels

Each detector is placed roughly  $2 \times 10^5 nm$  from the dimer (can be adjusted later for testing), with the position of the detector being defined by the polar and azimuth angles ( $\theta$  &  $\phi$  respectively) such that:

$$[x_{fiber}, y_{fiber}, z_{fiber}] = [r\cos(\phi)\sin(\theta), r\sin(\phi)\sin(\theta), r\cos(\theta)] \quad (5.11)$$

So if you were to place the fibers in the trapping frames x-y plane, in the probe beam frame will only have x and z components. The orientation of the detector is just the -ve of its position and not scaled by the distance term r, the orientation being the vector from the origin of the detector to the center of the dimer.

Pixels can be thought of as points lying on the surface of the detector, by getting

the spherical coordinates of each pixel we can compute the intensity at each point on the detector, allowing us to determine the average intensity on a given detector. The pixels are distributed using a sunflower distribution given by:

Where each point is first scaled to the size of the detector - for now we assume a radius of  $2.5 \times 10^4 \text{ nm}$  - and then translated from its position on the surface of the detector to the main coordinate system. Their orientation is treated much in the same as the detector's orientation, being its -ve position and scaled down by the radial distance from the dimer to the pixel, making it a unit vector. From their position we can also grab their spherical coordinates to create a list of points for mstm to evaluate. In order to accurately describe any detector surface we can use a Householder transformation to get the perpendicular circular surface of any vector.

This allows us to define the surface of any detector perpendicular to the origin of our coordinate system, we can freely choose the size and resolution of our fibre's. For every pixel we define the spherical coordinates relative to our origin, this is added to a list of  $\theta, \phi$  pairs that are evaluated by MSTM.

## 5.5 Interpretation of scattering data into orientation estimates

MSTM is capable of evaluating the scattering characteristics of a given target either in a fixed orientation or using an averaging of the particles orientation. While the latter method is satisfactory for simulation purposes it

## **Chapter 6**

## **Closing Remarks**

## **Appendix A**

### **Stuff That Didn't Fit Anywhere**

#### **Else**

# Bibliography

- [1] S. G. Agrawal and A. H. J. Paterson, “Secondary nucleation: Mechanisms and models,” *Chemical Engineering Communications*, vol. 202, no. 5, pp. 698–706, Jan. 2015.
- [2] A. Rohrbach and E. H. K. Stelzer, “Three-dimensional position detection of optically trapped dielectric particles,” *Journal of Applied Physics*, vol. 91, no. 8, pp. 5474–5488, Apr. 2002.
- [3] H. M. Schoen, C. S. Grove, and J. A. Palermo, “The early history of crystallization,” *Journal of Chemical Education*, vol. 33, no. 8, p. 373, Aug. 1956.
- [4] A. S. Myerson and R. Ginde, *Crystals, crystal growth, and nucleation*. Elsevier, 2002, pp. 33–65.
- [5] H. Fu, X. Gao, X. Zhang, and L. Ling, “Recent advances in nonclassical crystallization: Fundamentals, applications, and challenges,” *Crystal Growth amp; Design*, vol. 22, no. 2, pp. 1476–1499, Nov. 2021.
- [6] J. W. Mullin, *Crystallization.*, 4th ed. Oxford: Elsevier Science & Technology, 2001, description based on publisher supplied metadata and other sources.

## Bibliography

- [7] G. D. Botsaris, *Secondary Nucleation — A Review*. Springer US, 1976, pp. 3–22.
- [8] A. Cashmore, “Understanding and measurement of secondary nucleation,” Ph.D. dissertation, University of Strathclyde, 2022.
- [9] J. Frenkel, “A general theory of heterophase fluctuations and pretransition phenomena,” *The Journal of Chemical Physics*, vol. 7, no. 7, pp. 538–547, Jul. 1939.
- [10] M. Volmer and Weber, “Keimbildung in ubersattigten gebilden,” *Zeitschrift fur Physikalische Chemie*, vol. 119U, no. 1, pp. 277–301, Jan. 1926.
- [11] S. Karthika, T. K. Radhakrishnan, and P. Kalaichelvi, “A review of classical and nonclassical nucleation theories,” *Crystal Growth amp; Design*, vol. 16, no. 11, pp. 6663–6681, Oct. 2016.
- [12] R. Debuyschère, B. Rimez, A. Zacccone, and B. Scheid, “Experimental and theoretical investigation of nonclassical shear-induced nucleation mechanism for small molecule,” *Crystal Growth & Design*, vol. 23, no. 7, pp. 4979–4989, Jun. 2023.
- [13] F. Mura and A. Zacccone, “Effects of shear flow on phase nucleation and crystallization,” *Physical Review E*, vol. 93, no. 4, p. 042803, Apr. 2016.
- [14] D. Richard and T. Speck, “The role of shear in crystallization kinetics: From suppression to enhancement,” *Scientific Reports*, vol. 5, no. 1, Sep. 2015.
- [15] P. R. t. Wolde and D. Frenkel, “Enhancement of protein crystal nucleation by critical density fluctuations,” *Science*, vol. 277, no. 5334, pp. 1975–1978, Sep. 1997.

## Bibliography

- [16] O. Gliko, N. Neumaier, W. Pan, I. Haase, M. Fischer, A. Bacher, S. Weinkauf, and P. G. Vekilov, “A metastable prerequisite for the growth of lumazine synthase crystals,” *Journal of the American Chemical Society*, vol. 127, no. 10, pp. 3433–3438, Feb. 2005.
- [17] V. J. Anderson and H. N. W. Lekkerkerker, “Insights into phase transition kinetics from colloid science,” *Nature*, vol. 416, no. 6883, pp. 811–815, Apr. 2002.
- [18] J. R. Savage and A. D. Dinsmore, “Experimental evidence for two-step nucleation in colloidal crystallization,” *Physical Review Letters*, vol. 102, no. 19, p. 198302, May 2009.
- [19] K. G. Soga, J. R. Melrose, and R. C. Ball, “Metastable states and the kinetics of colloid phase separation,” *The Journal of Chemical Physics*, vol. 110, no. 4, pp. 2280–2288, Jan. 1999.
- [20] W. Ostwald, “Studien über die bildung und umwandlung fester körper: 1. abhandlung: Übersättigung und Überkaltung,” *Zeitschrift für Physikalische Chemie*, vol. 22U, no. 1, pp. 289–330, Feb. 1897.
- [21] A. Ashkin, J. M. Dziedzic, J. E. Bjorkholm, and S. Chu, “Observation of a single-beam gradient force optical trap for dielectric particles.”
- [22] A. Ashkin, “Applications of laser radiation pressure,” *Science*, vol. 210, no. 4474, pp. 1081–1088, Dec. 1980.
- [23] P.-W. Yi, W.-H. Chiu, T. Kudo, T. Sugiyama, R. Bresolí-Obach, J. Hofkens, E. Chatani, R. Yasukuni, Y. Hosokawa, S. Toyouchi, and H. Masuhara, “Cooper-

## Bibliography

- ative optical trapping of polystyrene microparticle and protein forming a submillimeter linear assembly of microparticle,” *The Journal of Physical Chemistry C*, vol. 125, no. 34, pp. 18 988–18 999, Aug. 2021.
- [24] J. Ahn, Z. Xu, J. Bang, Y.-H. Deng, T. M. Hoang, Q. Han, R.-M. Ma, and T. Li, “Optically levitated nanodumbbell torsion balance and ghz nanomechanical rotor,” *Physical Review Letters*, vol. 121, no. 3, p. 033603, Jul. 2018.
- [25] F. Monteiro, S. Ghosh, E. C. van Assendelft, and D. C. Moore, “Optical rotation of levitated spheres in high vacuum,” *Physical Review A*, vol. 97, no. 5, p. 051802, May 2018.
- [26] B. A. Garetz, J. E. Aber, N. L. Goddard, R. G. Young, and A. S. Myerson, “Non-photochemical, polarization-dependent, laser-induced nucleation in supersaturated aqueous urea solutions,” *Physical Review Letters*, vol. 77, no. 16, pp. 3475–3476, Oct. 1996.
- [27] B. A. Garetz, J. Matic, and A. S. Myerson, “Polarization switching of crystal structure in the nonphotochemical light-induced nucleation of supersaturated aqueous glycine solutions,” *Physical Review Letters*, vol. 89, no. 17, p. 175501, Oct. 2002.
- [28] X. Sun, B. A. Garetz, and A. S. Myerson, “Supersaturation and polarization dependence of polymorph control in the nonphotochemical laser-induced nucleation (nplin) of aqueous glycine solutions,” *Crystal Growth & Design*, vol. 6, no. 3, pp. 684–689, 2006.

## Bibliography

- [29] B. C. Knott, M. F. Doherty, and B. Peters, “A simulation test of the optical kerr mechanism for laser-induced nucleation,” *The Journal of Chemical Physics*, vol. 134, no. 15, Apr. 2011.
- [30] A. J. Alexander and P. J. Camp, “Single pulse, single crystal laser-induced nucleation of potassium chloride,” *Crystal Growth &amp; Design*, vol. 9, no. 2, pp. 958–963, Dec. 2008.
- [31] A. Goswami, I. S. Dalal, and J. K. Singh, “Seeding method for ice nucleation under shear,” *The Journal of Chemical Physics*, vol. 153, no. 9, Sep. 2020.
- [32] A. Mersmann, *Crystallization Technology Handbook*. CRC Press, May 2001.
- [33] J. D. Jackson, *Classical Electrodynamics*. New York: Wiley, 1975.
- [34] J. P. Gordon, “Radiation forces and momenta in dielectric media,” *Physical Review A*, vol. 8, no. 1, pp. 14–21, Jul. 1973.
- [35] T. A. Yasuhiro Harada, “Radiation forces on a dielectric sphere in the rayleigh scattering regime,” *Optics Communications*, vol. 124, no. 5-6, pp. 529–541, Mar. 1996. [Online]. Available: <https://www.sciencedirect.com/science/article/pii/0030401895007539>
- [36] P. C. Waterman, “New formulation of acoustic scattering,” *The Journal of the Acoustical Society of America*, vol. 45, no. 6, pp. 1417–1429, Jun. 1969.
- [37] T. Wriedt and U. Comberg, “Comparison of computational scattering methods,” *Journal of Quantitative Spectroscopy and Radiative Transfer*, vol. 60, no. 3, pp. 411–423, Sep. 1998.

## Bibliography

- [38] D. W. Mackowski and M. I. Mishchenko, “A multiple sphere t-matrix fortran code for use on parallel computer clusters,” vol. 112, pp. 2182–2192, 2011.
- [39] ——, “Calculation of the t matrix and the scattering matrix for ensembles of spheres,” *Journal of the Optical Society of America A*, vol. 13, no. 11, p. 2266, Nov. 1996.
- [40] Y.-l. Xu, “Electromagnetic scattering by an aggregate of spheres,” *Applied Optics*, vol. 34, no. 21, p. 4573, Jul. 1995.
- [41] E. M. Purcell and C. R. Pennypacker, “Scattering and absorption of light by nonspherical dielectric grains,” *The Astrophysical Journal*, vol. 186, p. 705, Dec. 1973.
- [42] G. H. Goedecke and S. G. O’Brien, “Scattering by irregular inhomogeneous particles via the digitized green’s function algorithm,” *Applied Optics*, vol. 27, no. 12, p. 2431, Jun. 1988.
- [43] D. T. Gillespie and E. Seitaridou, *The Fickian theory of diffusion*. Oxford University Press, Oct. 2012, pp. 1–17.
- [44] ——, *Einstein’s theory of diffusion*. Oxford University Press, Oct. 2012, pp. 38–53.
- [45] ——, *Langevin’s theory of diffusion*. Oxford University Press, Oct. 2012, pp. 174–190.
- [46] G. Volpe and G. Volpe, “Simulation of a brownian particle in an optical trap,” *American Journal of Physics*, vol. 81, no. 3, pp. 224–230, Feb. 2013.

## Bibliography

- [47] K. Berg-Sørensen and H. Flyvbjerg, “Power spectrum analysis for optical tweezers,” vol. 75, pp. 594–612, 2004.
- [48] S. B. Smith, Y. Cui, and C. Bustamante, *[7] Optical-trap force transducer that operates by direct measurement of light momentum*. Elsevier, 2003, pp. 134–162.
- [49] W. Vigilante, O. Lopez, and J. Fung, “Brownian dynamics simulations of sphere clusters in optical tweezers,” *Optics Express*, vol. 28, no. 24, p. 36131, Nov 2020.
- [50] M. Li and J. Arlt, “Trapping multiple particles in single optical tweezers,” vol. 281, pp. 135–140, 2008.
- [51] Yogesha, S. Bhattacharya, and S. Ananthamurthy, “Precise characterization of micro rotors in optical tweezers,” *arXiv: Soft Condensed Matter*, 2011. [Online]. Available: <https://api.semanticscholar.org/CorpusID:118262469>
- [52] T. A. Nieminen, V. L. Y. Loke, A. B. Stilgoe, G. Knöner, A. M. Brańczyk, N. R. Heckenberg, and H. Rubinsztein-Dunlop, “Optical tweezers computational toolbox,” vol. 9, pp. S196–S203, 2007.
- [53] O. Farsund and B. U. Felderhof, “Force, torque, and absorbed energy for a body of arbitrary shape and constitution in an electromagnetic radiation field,” *Physica A*, vol. 227, no. 1–2, p. 108–130, May 1996.
- [54] J. H. Crichton and P. L. Marston, “The measurable distinction between the spin and orbital angular momenta of electromagnetic radiation,” 2000. [Online]. Available: <https://api.semanticscholar.org/CorpusID:16957430>

## Bibliography

- [55] L. Friedrich and A. Rohrbach, “Tuning the detection sensitivity: a model for axial backfocal plane interferometric tracking,” *Opt. Lett.*, vol. 37, no. 11, pp. 2109–2111, Jun 2012. [Online]. Available: <https://opg.optica.org/ol/abstract.cfm?URI=ol-37-11-2109>
- [56] H.-I. Kim, I.-J. Joo, S.-H. Song, P.-S. Kim, K.-B. Im, and C.-H. Oh, “Dependence of the optical trapping efficiency on the ratio of the beam radius-to-the aperture radius,” *Journal of the Korean Physical Society*, vol. 43, no. 3, p. 348, 2003.
- [57] S. N. S. Reihani, M. A. Charsooghi, H. R. Khalesifard, and R. Golestanian, “Efficient in-depth trapping with an oil-immersion objective lens,” vol. 31, p. 766, 2006.
- [58] G. M. Gibson, J. Leach, S. Keen, A. J. Wright, and M. J. Padgett, “Measuring the accuracy of particle position and force in optical tweezers using high-speed video microscopy,” *Optics Express*, vol. 16, no. 19, p. 14561, Sep. 2008.
- [59] S. J. Parkin, R. Vogel, M. Persson, M. Funk, V. L. Loke, T. A. Nieminen, N. R. Heckenberg, and H. Rubinsztein-Dunlop, “Highly birefringent vaterite microspheres: production, characterization and applications for optical micromanipulation,” *Optics Express*, vol. 17, no. 24, p. 21944, Nov. 2009.
- [60] K. Saito and Y. Kimura, “Optically driven liquid crystal droplet rotator,” *Scientific Reports*, vol. 12, no. 1, Oct. 2022.
- [61] J. Millen, T. Deesuwan, P. Barker, and J. Anders, “Nanoscale temperature measurements using non-equilibrium brownian dynamics of a levitated nanosphere,”

## Bibliography

- Nature Nanotechnology*, vol. 9, no. 6, pp. 425–429, May 2014.
- [62] P. Rodríguez-Sevilla, Y. Arita, X. Liu, D. Jaque, and K. Dholakia, “The temperature of an optically trapped, rotating microparticle,” *ACS Photonics*, vol. 5, no. 9, pp. 3772–3778, Aug. 2018.
- [63] G. Knöner, S. Parkin, N. R. Heckenberg, and H. Rubinsztein-Dunlop, “Characterization of optically driven fluid stress fields with optical tweezers,” *Physical Review E*, vol. 72, no. 3, p. 031507, Sep. 2005.
- [64] R. M. Robertson-Anderson, “Optical tweezers microrheology: From the basics to advanced techniques and applications,” *ACS Macro Letters*, vol. 7, no. 8, pp. 968–975, Aug. 2018.
- [65] Y. Arita, J. M. Richards, M. Mazilu, G. C. Spalding, S. E. Skelton Spesyvtseva, D. Craig, and K. Dholakia, “Rotational dynamics and heating of trapped nanovaterite particles,” *ACS Nano*, vol. 10, no. 12, pp. 11 505–11 510, Dec. 2016.
- [66] A. I. Bishop, T. A. Nieminen, N. R. Heckenberg, and H. Rubinsztein-Dunlop, “Optical microrheology using rotating laser-trapped particles,” *Physical Review Letters*, vol. 92, no. 19, p. 198104, May 2004.
- [67] O. Y. Gowayed, T. Moosa, A. M. Moratos, T. Hua, S. Arnold, and B. A. Garetz, “Dynamic light scattering study of a laser-induced phase-separated droplet of aqueous glycine,” vol. 125, pp. 7828–7839, 2021.
- [68] Z. Liao and K. Wynne, “A metastable amorphous intermediate is responsible for laser-induced nucleation of glycine,” vol. 144, pp. 6727–6733, 2022.

## Bibliography

- [69] F. Walton and K. Wynne, “Control over phase separation and nucleation using a laser-tweezing potential,” vol. 10, pp. 506–510, 2018.
- [70] T. Rungsimanon, K. ichi Yuyama, T. Sugiyama, and H. Masuhara, “Crystallization in unsaturated glycine/ $\text{d}_{\text{j}}\text{s}\text{u}\text{b}\{\text{j}2\text{j}\}/\text{s}\text{u}\text{b}\{\text{j}0$  solution achieved by irradiating a focused continuous wave near infrared laser,” vol. 10, pp. 4686–4688, 2010.
- [71] S. Xu, Y. Li, and L. Lou, “Axial optical trapping forces on two particles trapped simultaneously by optical tweezers,” vol. 44, p. 2667, 2005.
- [72] P. Praveen, Yogesha, S. S. Iyengar, S. Bhattacharya, and S. Ananthamurthy, “Two particle tracking and detection in a single gaussian beam optical trap,” vol. 55, p. 585, 2016.
- [73] J. C. Loudet, B. M. Mihiretie, and B. Pouliquen, “Optically driven oscillations of ellipsoidal particles. part ii: Ray-optics calculations,” vol. 37, 2014.
- [74] X. Sheng-Hua, L. Yin-Mei, L. Li-Ren, and S. Zhi-Wei, “Computer simulation of the collision frequency of two particles in optical tweezers,” vol. 14, pp. 382–385, 2005.
- [75] C. D, P. P, N. B V, S. Bhattacharya, and S. Ananthamurthy, “Laser polarization driven micromanipulation and reorientation dynamics of an asymmetric shaped microscopic biomaterial using optical tweezers,” *Journal of Optics*, vol. 24, no. 9, p. 094007, Aug. 2022.

## Bibliography

- [76] A. A. Ranha Neves and C. L. Cesar, “Analytical calculation of optical forces on spherical particles in optical tweezers: tutorial,” *Journal of the Optical Society of America B*, vol. 36, no. 6, p. 1525, May 2019.
- [77] V. Shahabadi and E. Madadi, “Effective multiple optical trapping of sub-micrometer particles with petal beams,” *Journal of the Optical Society of America B*, vol. 37, no. 12, p. 3665, Nov. 2020.
- [78] R. Reimann, M. Doderer, E. Hebestreit, R. Diehl, M. Frimmer, D. Windey, F. Tebbenjohanns, and L. Novotny, “Ghz rotation of an optically trapped nanoparticle in vacuum,” *Physical Review Letters*, vol. 121, no. 3, p. 033602, Jul. 2018.
- [79] A. Yevick, D. J. Evans, and D. G. Grier, “Photokinetic analysis of the forces and torques exerted by optical tweezers carrying angular momentum,” *Philosophical Transactions of the Royal Society A: Mathematical, Physical and Engineering Sciences*, vol. 375, no. 2087, p. 20150432, Feb. 2017.
- [80] Q. Zhu, N. Li, H. Su, W. Li, and H. Hu, “Dynamic analysis and simulation of an optically levitated rotating ellipsoid rotor in liquid medium,” *Photonic Sensors*, vol. 12, no. 2, pp. 105–116, Sep. 2021.
- [81] M. Rashid, M. Toroš, A. Setter, and H. Ulbricht, “Precession motion in levitated optomechanics,” *Physical Review Letters*, vol. 121, no. 25, p. 253601, Dec. 2018.
- [82] T. M. Hoang, Y. Ma, J. Ahn, J. Bang, F. Robicheaux, Z.-Q. Yin, and T. Li, “Torsional optomechanics of a levitated nonspherical nanoparticle,” *Physical Review Letters*, vol. 117, no. 12, p. 123604, Sep. 2016.

## Bibliography

- [83] S. Kuhn, A. Kosloff, B. A. Stickler, F. Patolsky, K. Hornberger, M. Arndt, and J. Millen, “Full rotational control of levitated silicon nanorods,” 2016.